CONTROLLER DESIGN AND IMPLEMENTATION FOR A 6-DEGREE-OF-FREEDOM MAGNETICALLY LEVITATED POSITIONER WITH HIGH PRECISION

A Thesis

by

HO YU

Submitted to the Office of Graduate Studies of
Texas A&M University
in partial fulfillment of the requirements for the degree of

MASTER OF SCIENCE

August 2005

Major Subject: Mechanical Engineering

CONTROLLER DESIGN AND IMPLEMENTATION FOR A 6-DEGREE-OF-FREEDOM MAGNETICALLY LEVITATED POSITIONER WITH HIGH PRECISION

A Thesis

by

HO YU

Submitted to the Office of Graduate Studies of
Texas A&M University
in partial fulfillment of the requirements for the degree of

MASTER OF SCIENCE

Approved by:

Chair of Committee,	Won-jong Kim
Committee Members,	Alexander Parlos
	James G. Boyd
Head of Department,	Dennis O'Neal

August 2005

Major Subject: Mechanical Engineering

ABSTRACT

Controller Design and Implementation for a 6-Degree-of-Freedom

Magnetically Levitated Positioner with High Precision.

(August 2005)

Ho Yu, B.S., Hanyang University, Korea

Chair of Advisory Committee: Dr. Won-jong Kim

This thesis presents the controller design and implementation of a high-precision 6-degree-of-freedom (6-DOF) magnetically levitated (maglev) positioner. This high-precision positioning system consists of a novel concentrated-field magnet matrix and a triangular single-moving part that carries three 3-phase permanent-magnet linear-levitation-motor armatures. Since only a single levitated moving part, namely the platen, generates all required fine and coarse motions, this positioning system is reliable and low-cost. Three planar levitation motors based on the Lorentz-force law not only generate the vertical force to levitate the triangular platen but control the platen's position and orientation in the horizontal plane. All 6-DOF motions are controlled by magnetic forces only. The platen is regarded a pure mass system, and the spring and damping coefficients are neglected except for the vertical directions. Single-input single-output (SISO) digital lead-lag controllers are designed and implemented on a digital signal processor (DSP). This 6-DOF fully magnetically levitated positioner has a total mass of 5.91 kg and currently exhibits a 120 mm × 120 mm travel range. This positioner is highly suitable for semiconductor-manufacturing applications such as wafer steppers. Several experimental motion profiles are presented to demonstrate the maglev stage's capability of accurately tracking any planar and 3-D paths.

ACKNOWLEDGMENTS

First, I give my sincere gratitude to my advisor, Dr. Won-jong Kim, for his advice and encouragement during my Master of Science course. I am very appreciative of the valuable opportunity to study in the Nano Mechatronics Lab at Texas A&M University. I admire his knowledge and experience about electrical systems and precision positioning systems.

I thank Dr. Alexander Parlos and Dr. James G. Boyd who are my committee members. I really appreciate them for giving me great advice and consideration about my master's program.

I give thanks to my parents, Mr. Seok-jong Yu and Mrs. In-sun Kim. They always encourage and love me.

Nikhil Bhat, a former master's student of Dr. Won-jong Kim, did the mechanical design of the positioner and magnet matrix. Tiejun Hu, a former doctorial student of Dr. Won-jong Kim completed the construction of the integrated multidimensional positioner. This material is in part based upon work supported by The Texas Advanced Technology Program under Grant 000512 - 0225-2001.

TABLE OF CONTENTS

Page

ABSTRACT iii

ACKNOWLEDGMENTS iv

TABLE OF CONTENTS v

LIST OF FIGURES vii

LIST OF TABLES x

CHAPTER I INTRODUCTION 1

1.1 High-Precision Motion Control 1
1.1.1 Prior Art 1
1.2 Levitation Technology 2
1.2.1 Aerodynamic Levitation 3
1.2.3 Magnetic Levitation 3
1.3 Overview of Magnetic Levitation Stage 4
1.4 Thesis Overview 10
1.5 Thesis Contributions 11

CHAPTER II OVERVIEW OF MAGNETICALLY LEVITATED POSITIONER 12

2.1 Analysis for Electromagnetic System 12
2.1.1 Halbach Magnet Array 12
2.1.2 Concentrated-Field Magnet Matrix 13
2.2 Linear Motor 14
2.2.1 Sawyer Motor 14
2.2.2 Synchronous-Permanent-Magnet Planar Motor 14
2.2.3 Working Principle of Maglev Positioner 15
2.3 Instrumentation Structure 15
2.3.1 Sensors 19
2.3.2 Digital Signal Processor 23
2.4 Control Structure 23

CHAPTER III DYNAMIC MODELLING 25

3.1 Mass and Inertia Tensor of the Platen 25

Page

3.2 Specification of Positioner 26
3.3 Decoupled Equations of Motion 27
3.3.1 *DQ* decomposition 27
3.3.2 Linearized Force Equations 28
3.3.3 Vertical Equations of Motion 29
3.3.4 Lateral Equations of Motion 29
3.4 Dynamic Model of System 30
3.4.1 Linearized Equations of Motion in Horizontal and Vertical Modes.. ... 30
3.4.2 Sensor Equation 33

CHAPTER IV CONTROLLER DESIGN 38

4.1 Digital Controller Design Procedure 38
4.1.1 Controller for Vertical Mode 38
4.1.2 Controller for Lateral Mode 47

CHAPTER V 6-DOF CLOSED-LOOP EXPERIMENTAL RESULTS 48

5.1 Experimental Setup 48
5.2 Step Responses 51
5.3 Large-Range Trajectory Scanning Motions 62

CHAPTER VI CONCLUSIONS AND SUGGESTIONS FOR FUTURE WORK 66

6.1 Conclusions 66
6.2 Suggestions for Future Work 67

REFERENCES 69

APPENDIX REAL-TIME CONTROL C CODE 71

VITA……...……..…91

LIST OF FIGURES

FIGURE Page

1-1 Schematic view of the 6-degree-of-freedom wafer stepper stage……..……2

1-2 Aerodynamic levitation for multidimensional positioner……..…4

1-3 Photograph of 6-DOF maglev positioner with high precision……..…5

1-4 Perspective view of the positioner……..……7

1-5 Perspective bottom view of the positioner……..7

1-6 Photograph of magnet matrix…….……..8

1-7 Diagram of 6-DOF motion generation (a) the overview, (b)x, (c)y, (d)ϕ, (e)z, (f)θ, and (g)ψ ……..…….....9

2-1 Superimposition of the two orthogonal Halbach magnet arrays. (b) Top view of the concentrated-field magnet matrix…..……13

2-2 Perspective views of integrated multi-dimensional positioner concepts. (a) Moving magnet-stationary-winding design. (b) Moving-winding-stationary -magnet design…….…..…16

2-3 Working principle of the integrated multidimensional positioning technology. (a) y-directional motion generation. (b) Diagonal motion generation……...16

2-4 Schematic diagram of the instrumentation structure……17

2-5 (a) Whole VME system, (b) ADE 3800 boards and power supplies, and (c) VME 7751 VME PC, Pentek DSP board, Pentek 6102 data acquisition board, VME chassis, Agilent 10897B laser axis boards, and power amplifier……..…18

2-6 Laser interferometer setup……20

2-7 (a) Laser head (HP 5517D), and (b) Laser interferometer and mount..... 21

FIGURE Page

2-8 (a) Nanogage 100 laser distance sensor, (b) side view of the vertical sensor mount, and (c) bottom view of the vertical sensor mount..... 22

2-9 Schematic diagram of the control structure.....24

3-1 *DQ* coordinates attached to the platen.....28

3-2 Individual force components generated by motors *A*, *B*, and *C*.....31

3-3 Schematic view of laser interferometers.....34

3-4 Position of laser distance sensors.....36

4-1 Root locus.....40

4-2 Block diagram for the lead-lag controller.....40

4-3 Loop transmission for z.....41

4-4 Closed-loop Bode plot for z.....42

4-5 Root locus for θ.....44

4-6 Loop transmission for θ.....45

4-7 Closed-loop Bode plot for θ.....46

5-1 (a) Initial setting with shims of 0.04-inch-thick and (b) after magnetic levitation without shims.....49

5-2 Initial working position of the positioner.....50

5-3 10-μm *x*-axis step response at a 20-μm levitation height with perturbations in other axes.....52

5-4 5-μm *x*-axis step response at a 20-μm levitation height with perturbations in other axes.....53

5-5 30-μm *x*-axis step response at a 30-μm levitation height with perturbations in other axes 54

FIGURE Page

5-6 10-µm *y*-axis step response at a 40-µm levitation height with perturbations in other axes……...55

5-7 20-µm *y*-axis step response at a 40-µm levitation height with perturbations in other axes ……..……....56

5-8 5-µm *z*-axis step response at a 10-µm levitation height with perturbations in other axes….……..…….57

5-9 10-µm *z*-axis step response at a 15-µm levitation height with perturbation in other axes….……..58

5-10 20-µrad θ-axis step response at a 71-µm levitation height with perturbation in other axes…..…….……59

5-11 20-µrad φ -axis step response at a 71-µm levitation height with perturbation in other axes……...……...…….60

5-12 20-µrad ψ-axis step response at a 71-µm levitation height with perturbation in other axes……...61

5-13 (a) 50-µm step response in *x* and (b) its FFT. (c) 100-µm step response in *x* and (d) its FFT……..……..62

5-14 Capability of following paths. (a) 5-mm radius circular motion (b) star-shape motion……...……....63

5-15 120-mm maximum travel range in (a) *x* and (b) *y* ……..….64

5-16 1-µm amplitude sinusoidal motion…….……64

5-17 500-µm radius spring-shape trajectory in 3-D……..……..…..65

5-18 Velocity profiles in *y* with a 0.025-m/s maximum velocity……....65

LIST OF TABLES

TABLE Page

3-1 6-DOF motions generated by the linear motors……...31

3-2 Values of length variables in Figure 3-4……..37

CHAPTER I

INTRODUCTION

1.1 High-Precision Motion Control

In modern nanoscale or microscale engineering, wafer steppers, surface profilometers, and scanned probe microscopes require high-precision motion control. Especially the wafer stepper stage in semiconductor manufacturing is the main application of the work presented in this thesis. Figure 1-1 shows a schematic of a wafer stage in integrated-circuit (IC) fabrication. The wafer stepper stage is very important equipment for photolithography such as generating step-and-repeat motions. An optical source sheds a deep-ultraviolet (DUV) beam through the mask onto each die site on the wafer. The wafer stage is required to move the wafer in all 6 directions with minimum errors. In the same time, it should have high resolution and accuracy, long travel range, multidimensional performance, and high control bandwidth, minimizing mechanical vibrations. In this thesis, a 6-degree-of-feedom (DOF) maglev positioner with high precision is presented for a future wafer stage in the semiconductor manufacturing industry.

1.1.1 Prior Art

Conventional precision positioners used in industry are the crossed-axis type and the gantry type. The crossed-axis type has a stage for one axis on another. The moving parts are usually controlled by stepper motors and ball screws. In order to reduce friction, some positioners employ air-bearings in spite of their complicated design. The gantry type has a bridge-like frame.

This thesis follows the style of *American Society of Mechanical Engineering*.

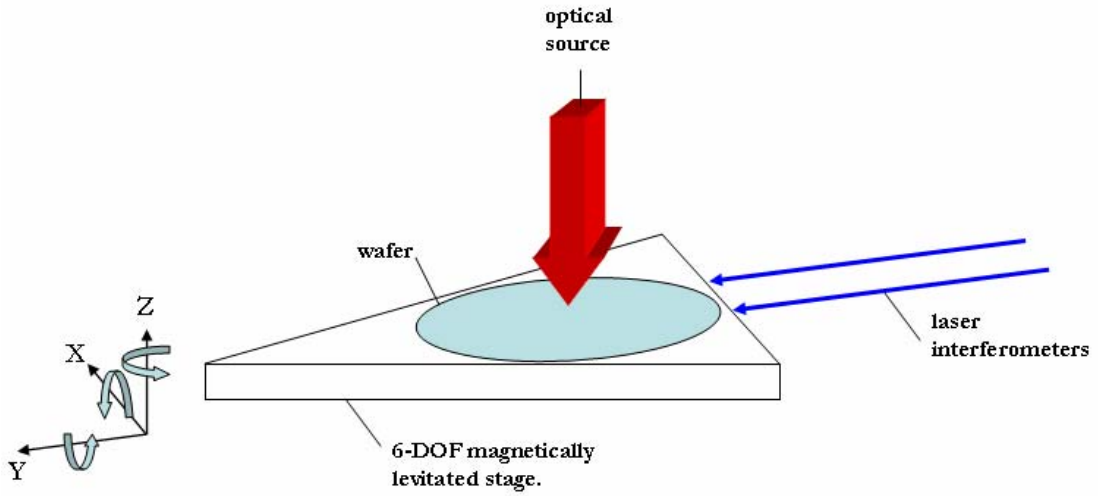

Figure 1-1 Schematic of a 6-degree-of-freedom wafer stepper stage

The mover is controlled by two motors at the end of the bridge. This kind of positioners is used in scanners and plotters without high positioning resolution. These traditional precision positioners have significant drawbacks including inherently not being able to generate rotational motions. Although rotational motions could be added by extra devices, the whole positioner would have been more complicated and bulkier. It is because each direction of motion requires individual actuators. As a result, the whole positioning system may exhibit dynamic coupling and may be difficult to control. [1–4].

1.2 Levitation Technology

The friction between moving parts can be one of the obstacles in micro- or submicro-scale control. In order to overcome friction, some levitation methods were suggested in industry. Here, levitation is defined as a phenomenon where there is no mechanical contact. The levitation technology would be crucial in the precision manufacturing industry. This thesis introduces a 6-degree-of-freedom maglev positioner for future precision manufacturing [5–6]. In the following

section, two cases of levitation (aerostatic and magnetic levitation) relevant to my research are presented.

1.2.1 Aerostatic Levitation

Tiejun Hu, a former PhD student of Dr. Won-jong Kim demonstrated the multidimensional levitation positioner with aerostatic bearings [1]. Figure 1-2 shows a schematic for aerostatic levitation. Air is injected through small nozzles on a bearing pad, which generates the suspension force against gravity. He chose the three air bearings (FP-C-010) manufactured by Nelson Air Corporation. These bearings have nominal 25-μm air gaps which a 20~90-psi air supply. The air supply is divided in three ways by a distributor. Low-cost manufacturing and high reliabilities are significant benefit of this technique whereas it has restrictions in the size of the air gaps and is subject to disturbances from turbulent flow.

1.2.2 Magnetic Levitation

Magnetic levitation has been developed for several applications like maglev high-speed trains, magnetic bearings, electromagnetic launchers, and superconducting gyroscopes [7]. Since no mechanical contact exists between a frame and a mover, the resolution, one of the most important factors in precision engineering, can be improved in the high-precision positioner presented in this thesis. The three magnetic planar motors operate based on the Lorentz force law. All 6-axis motions can be generated by the interaction of the three planar motors.

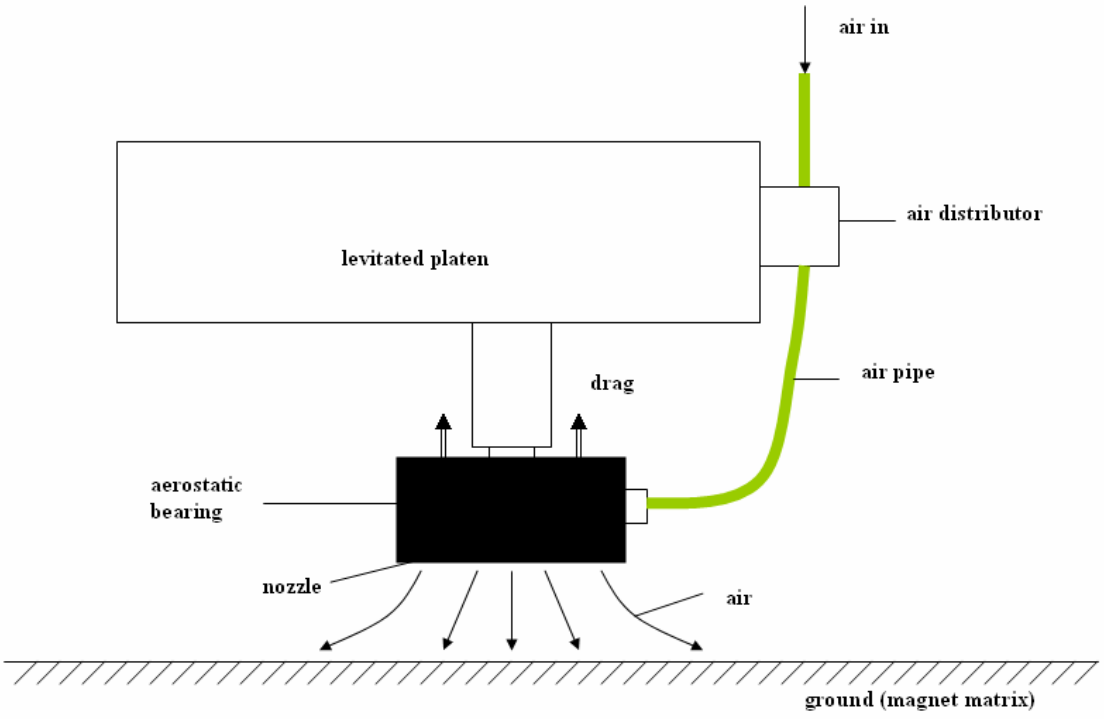

Figure 1-2 Aerostatic levitation for a multidimensional positioner

1.3 Overview of Magnetic Levitation Stage

Figure 1-3 shows a photograph of the 6-DOF maglev positioner with high precision. It consists of a sigle moving platen, which three planar motors and two plane mirrors, the base plate with a magnet matrix, three laser distance sensors, and three laser interferometers. Figures 1-4 and 1-5 represent perspective top and bottom views of the positioner, respectively. This positioner uses synchronous permanent-magnet planar motors (SPMPM) served as actuators, which are able to overcome the shortcomings of traditional planar motors [1]. The most significant feature is that the only one levitated moving part, namely the platen, can generate all 6-DOF fine and coarse motions. In addition, there are several additional advantages such as:

1. A mechanically non-contact machine structure does not need lubricants, nor produce wear particles. Therefore, it is suited for clean-room environment.

2. Superimposing multiple linear motors as one actuator reduces the footprint.

3. Compared to traditional positioners, the single moving frame can have high natural frequencies.

4. The simple design eliminates complicate components and reduces manufacturing cost with high reliability. [5–7]

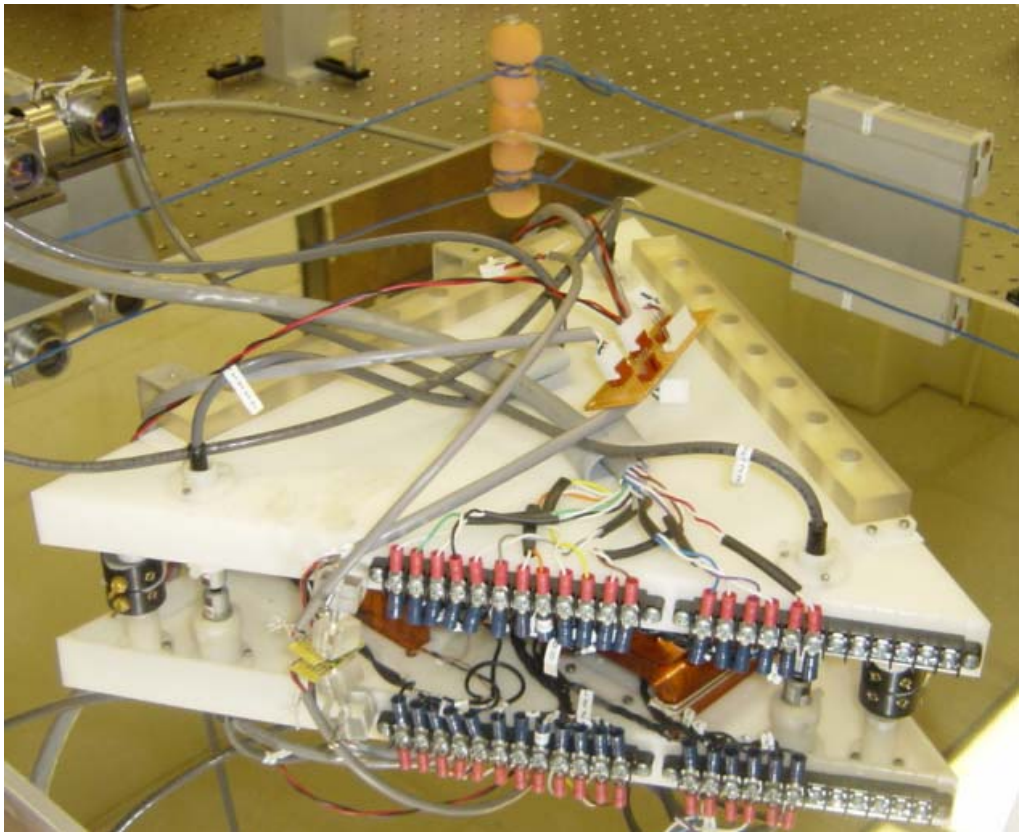

Figure 1-3 Photograph of 6-DOF maglev positioner with high precision

This positioner has a 5.91 kg platen mass and a 120 mm × 120 mm experimental maximum planar travel range. The frame of the platen was made of Delrin with a mass density of 1.54 g/cm² in order to reduce its total mass. The triangular design was chosen for the design simplicity. The magnet matrix, a superimposed concentrated-field double-axis magnet matrix shown in Figure 1-6 serves as a stator. The dimension of magnet matrix is 304.8 mm × 304.8 mm × 12.7 mm. The high-precision stick mirrors (manufactured by Bond optics) which reflect the laser beams are used for detecting the platen's planar displacement and velocity with laser interferometers.

Figure 1-7 defines the forces generated by the three planar motors. Any 6-DOF motions can be generated by a combination of these 6 force components. We define that (b) *x* means the *x*-axis motion, generated by motor *B* with other motors *A*, *C* canceling the error torque, (c) *y* represents the *y*-axis motion generated by motors *A* and *C*, and (d) ϕ denotes the rotation around the *z*-axis made by all of three motors. These *x*, *y*, and ϕ are horizontal motions and the following *z*, θ, and ψ are vertical motions. (e) *z* means the translation in *z* generated by all of the three motors in the same vertical directions, (f) θ is the rotation around the *x*-axis, and (g) ψ is the rotation around the *y*-axis, respectively.

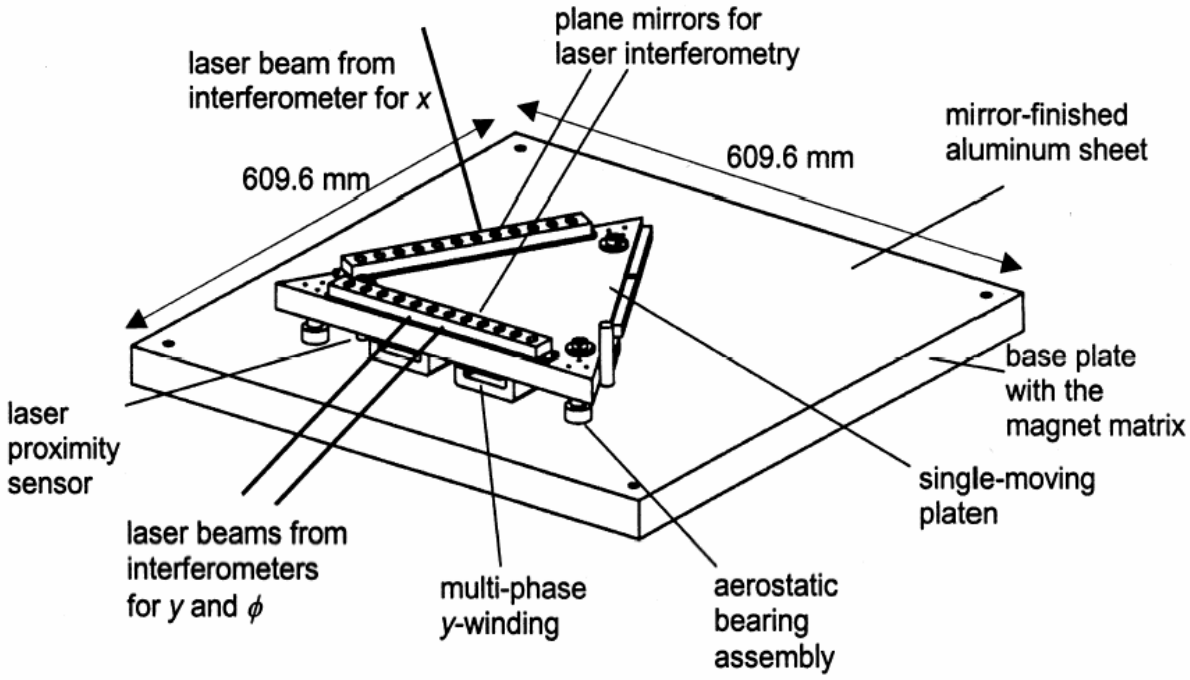

Figure 1-4 Perspective view of the positioner [1]

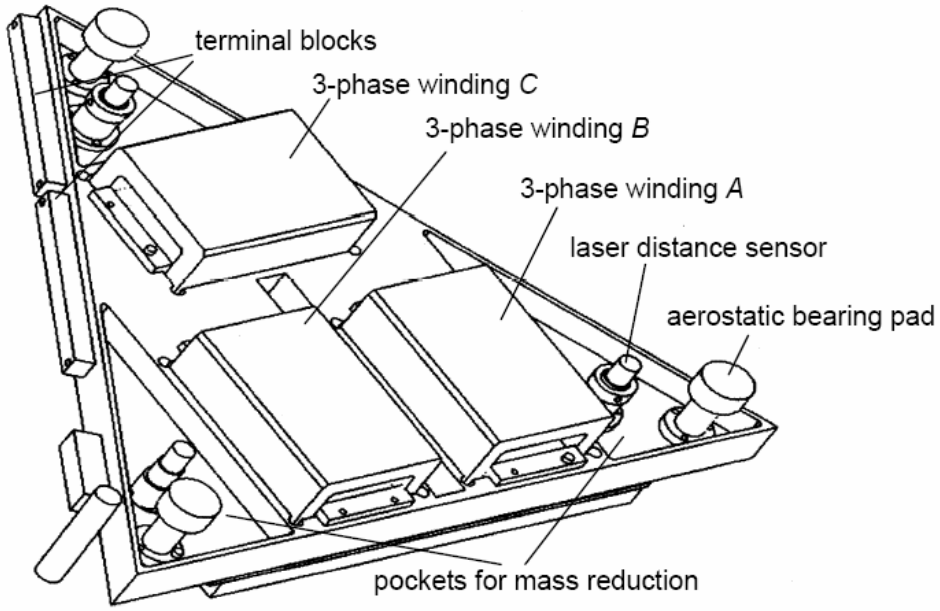

Figure 1-5 Perspective bottom view of the positioner [5]

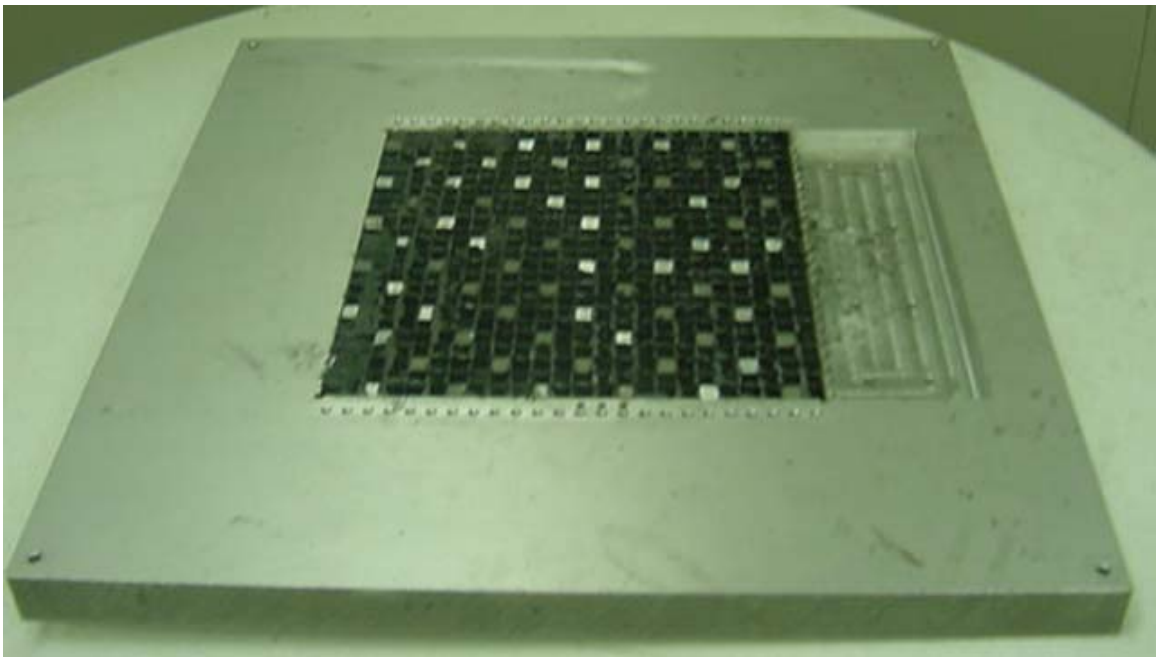

Figure 1-6 Photograph of magnet matrix [5]

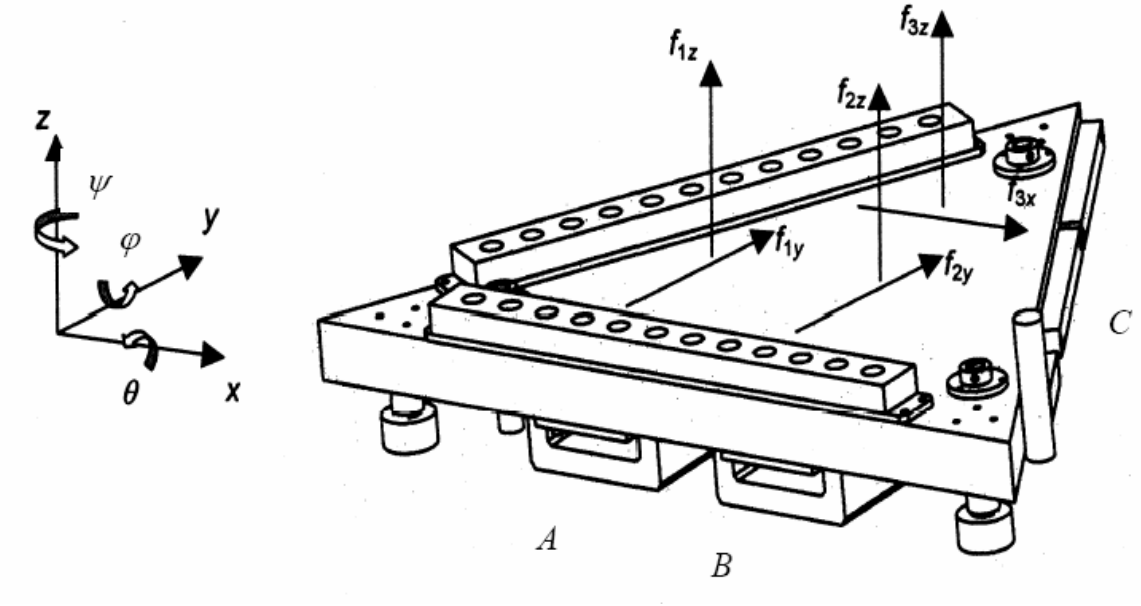

(a)

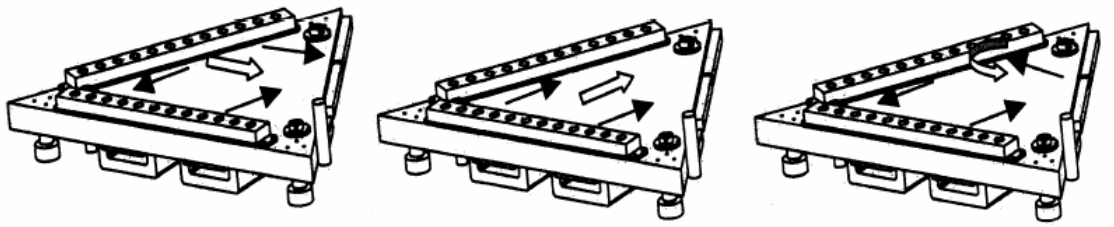

(b) (c) (d)

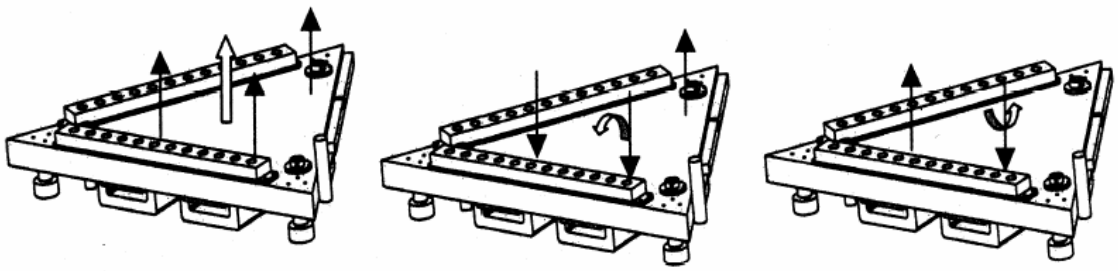

(e) (f) (g)

Figure 1-7 Diagram of 6-DOF motion generation (a) the overview, (b)*x*, (c)*y*, (d) ϕ , (e)*z*, (f) θ , and (g) $_{\psi}$

[1].

1.4 Thesis Overview

This thesis consists of six chapters: introduction, overview of magnetically levitated positioner, dynamic modeling, controller design, 6-DOF closed-loop experimental result, and conclusions and future work.

Chapter I introduces the reviews of precision engineering and its application examples. The introductions of levitation theory are illustrated, and the overview of the proposed 6-DOF magnetically levitated positioner with high precision is mentioned.

Chapter II presents the electromagnetic concepts for 6-DOF precision positioner. It includes the magnet matrix theory, overview of the planar motors, and the VME system controlling the positioner. The VMEbus (Versa Module Eurocard bus) based instrumentation and control structures for interface between digital signal processor and positioner are provided.

Chapter III describes several parameters and specifications required to control the precision positioner. Dynamic models of the levitator based on the Newton's second law are derived. In addition, *DQ* decomposition to remove nonlinearily in dynamics is applied, and linearlized state-space models in vertical and lateral modes are designed.

Chapter IV presents controller design procedures and implementation for the maglev system. Chapter V provides the 6-DOF closed-loop experimental results including micro- and nano-scale stepping motions, large-range travel motions in precision motion control such as semiconductor manufacturing.

Chapter VI gives the conclusions of this thesis and suggestions for future work. Reference is followed and C program code is included in the Appendix.

1.5 Thesis Contributions

This thesis presents maglev controller design, implementation, and experimental results. Nikhil Bhat and Tiejun Hu, former students of Dr. Won-jong Kim constructed the integrated multidimensional precision positioner with air-bearings [5–6]. After testing the air-bearing-levitated positioner to apply magnetic levitation, I designed controllers for 6-DOF magnetic levitation. For the *x*, *y*, and ϕ control algorithm and digital implementation SISO lead-lag control methods similar to the previous Hu's work are used [1]. In order to design the *z*-direction control, the positioner was first run in open loop in θ and φ. Then it was tested many times to select the best controller design. Several experimental results of nanometer- and sub-micrometer-level positioning are presented in this thesis.

CHAPTER II

OVERVIEW OF MAGNETICALLY LEVITATED POSITIONER

This chapter describes the electromagnetic principles of the magnet matrix and the planar motors used in the 6-DOF precision positioner. The VMEbus-based instrumentation structure and the control structure for the interface between the DSP and the positioner are also introduced.

2.1 Analysis for Electromagnetic System

2.1.1 Halbach Magnet Array

This magnetic array was first proposed by Halbach for use in undulators and particle accelerators [7]. This magnetic array has the remarkable property of primarily single-sided magnet field. Unlike conventional magnet arrays, the magnetization of each adjacent magnet segment is turned by a predetermined angle, 90˚ or 45˚. With the same volume, a linear Halbach array shows $\sqrt{2}$ times stronger field than that of a conventional ironless magnet array, thereby doubling the power efficiency of the linear motor or reducing the magnet mass [8]. Figure 2-1 (a) shows two Halbach arrays with magnetization rotated by 90˚ in each successive block.

2.1.2 Concentrated-Field Magnet Matrix

Figure 2-1 is the novel concentrated-field magnet matrix made by superimposition of two orthogonal Halbach arrays [7–8]. It generates permanent magnetic field in order to control the platen motion. Figure 2-1 (b), magnet blocks with an arrow have $1/\sqrt{2}$ times remanence compared to the magnets indicated at North and South poles. Blank block means the cancellation of the magnetic fields.

The whole magnet matrix has 6 pitches in the *x*- and *y*-directions respectively in this prototype design, and the stage has the maximum of 160 mm × 160 mm planar travel range. By increasing the size of the magnet matrix array, the travel range of the stage can be extended.

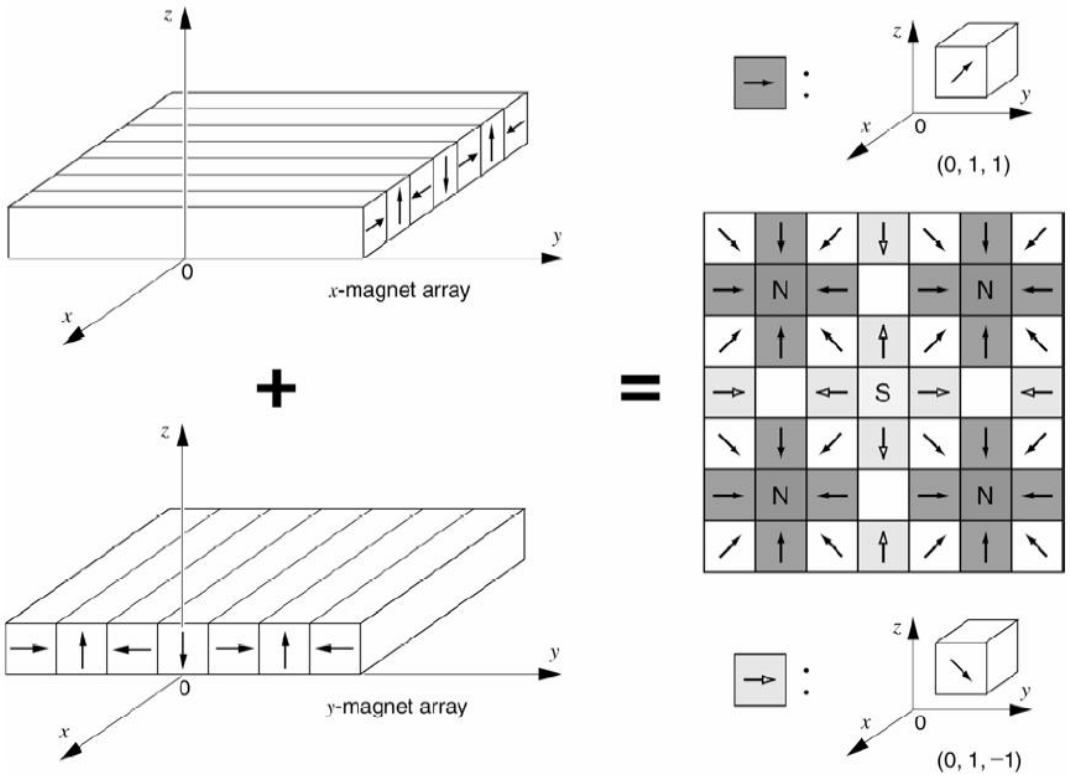

(a) (b)

Figure 2-1 (a) Superimposition of the two orthogonal Halbach magnet arrays. (b) Top view of the concentrated-field magnet matrix [7-8]

2.2 Linear Motor

The Sawyer motor and the synchronous permanent magnet planar motor (SPMPM) and the working principle of the maglev positioner are presented in this section.

2.2.1 Sawyer Motor

A Sawyer motor [9–12], the first variable-reluctance-type planar motor has been used in wafer probing and automated assembly. It consists of many square protrusions (teeth) from the superimposition of two orthogonal linear variable reluctance motors. Hinds and Nocito [11] and Pelta [12] improved the original version of the Sawyer motor for precision motion control applications, which is adjustable for wafer stepper stages

2.2.2 Synchronous Permanent-Magnet Planar Motor

A permanent-magnet-matrix motor uses a number of permanent-magnet cubes instead of iron protrusions as in a Sawyer motor in the base plate. This permanent-magnet matrix forms a stator in cross-stripe patterns. If the current flows in the windings attached to the bottom surface of the platen, magnetic force is generated. Asakawa proposed the first permanent-magnet planar motor [9–10]. He used the superimposition method with two orthogonal conventional one-dimensional magnet arrays. The 6-DOF maglev positioner presented in this thesis uses a superimposed Halbach magnet matrix shown in the Figure 2-1. This motor structure is also called a synchronous permanent-magnet planar motor (SPMPM) and shows improved features compared to the Sawyer motor and traditional permanent-magnet planar motor. This motor can generate all fine and coarse motions with only one levitated platen [9–15].

2.2.3 Working Principle of Maglev Positioner

Figure 2-2 (a), one of the maglev positioner concepts, shows that a two-dimensional superimposed concentrated-field magnet matrix is attached on the bottom surface of the moving part. On the other hand, another positioner is shown in Figure 2-2 (b) that carries the windings on the bottom of the platen with a magnet matrix base. Figure 2-3 demonstrates the working principle. For better understanding, the *x*- and *y*-direction windings are represented as sinusoidal waves of the magnetic field. Figure 2-3 (a) shows *y*-directional motion generation and (b), diagonal motion generation. In case of Figure 2-3 (a), only *y*-directional sinusoidal magnetic field is generated. There is no commutation in *x*. In case of Figure 2-3 (b), both *x*- and *y*-directional sinusoidal magnetic fields are generated by the windings simultaneously. As a result, the platen makes a diagonal motion.

2.3 Instrumentation Structure

The overall schematic diagram of the instrumentation structure of the 6-DOF maglev postitioner is showed in Figure 2-4. The digital control algorithms are implemented on the TMS320C40 (DSP) on a Pentek 4284 board. The VMEbus-based PC (VMIC 7751) and the DSP communicate with dual-port memory on the Pentek 4284 board. The VME PC works for user interface, which shows the platen's real-time states with several control variables. A VME system includes the VME PC, three laser-axis boards (Agilent 10897B), a 16-bit data-acquisition board (Pentek 6102), and a DATEL DVME-622 D/A converter board with the DSP board, as shown in Figure 2-5. The VME PC runs an interrupt service routine (ISR) written in C, and the user interface carries out transferring data to the DSP in real time.

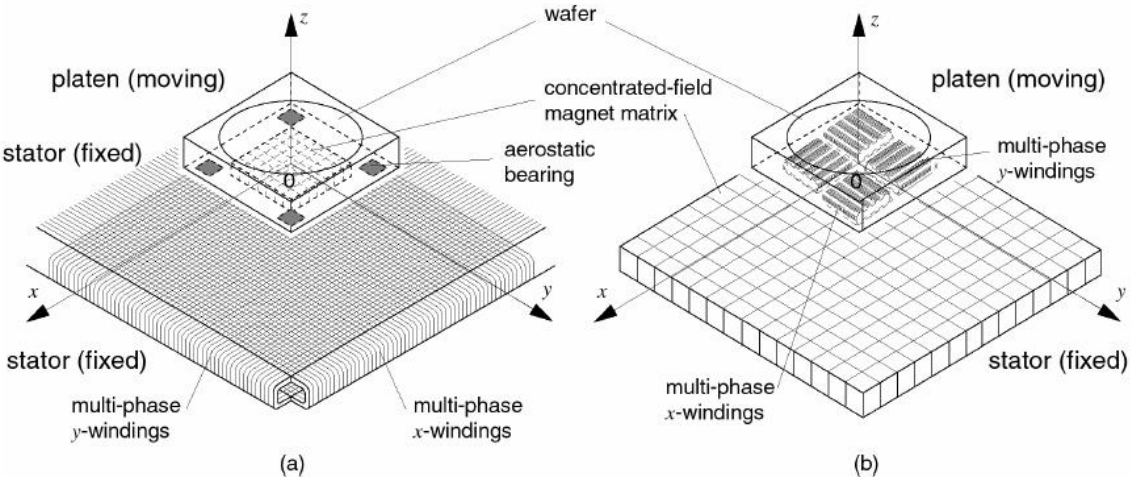

Figure 2-2 Perspective views of integrated multi-dimensional positioner concepts. (a) Moving magnet-stationary-winding design. (b) Moving-winding-stationary-magnet design [7]

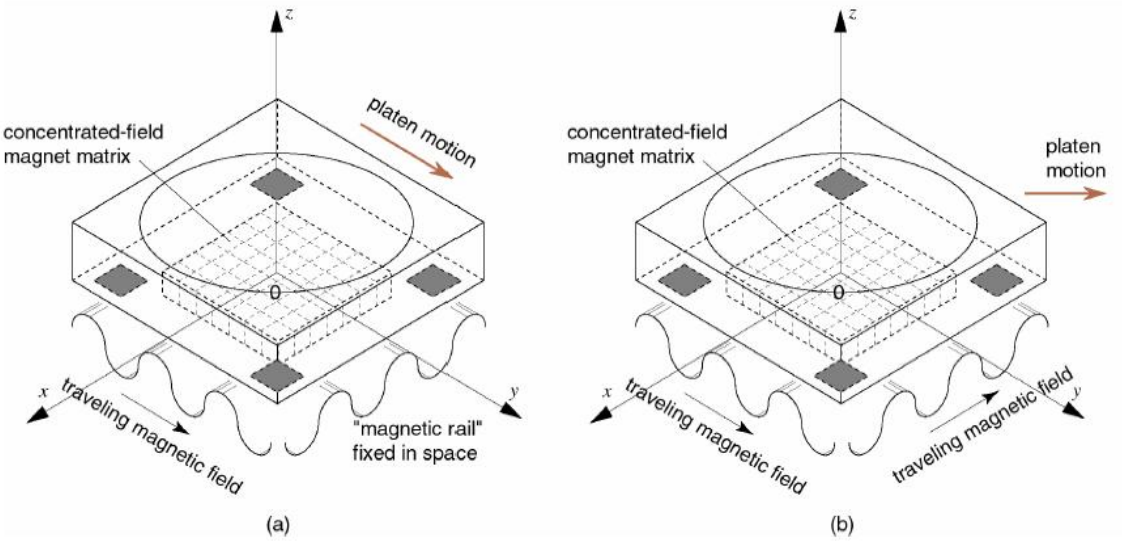

Figure 2-3 Working principle of the integrated multidimensional positioning technology. (a) *y*-directional motion generation. (b) Diagonal motion generation. [7]

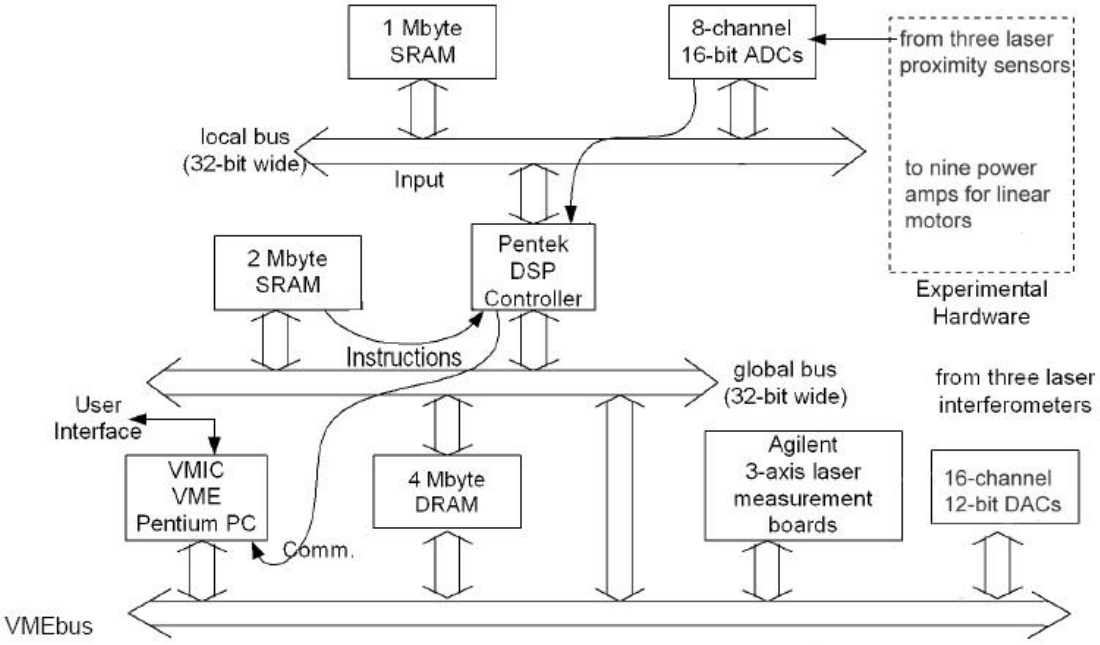

Figure 2-4 Schematic diagram of the instrumentation structure [1]

(a)

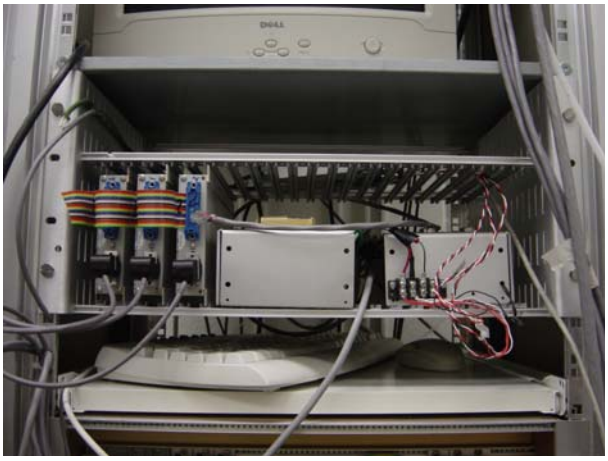

(b)

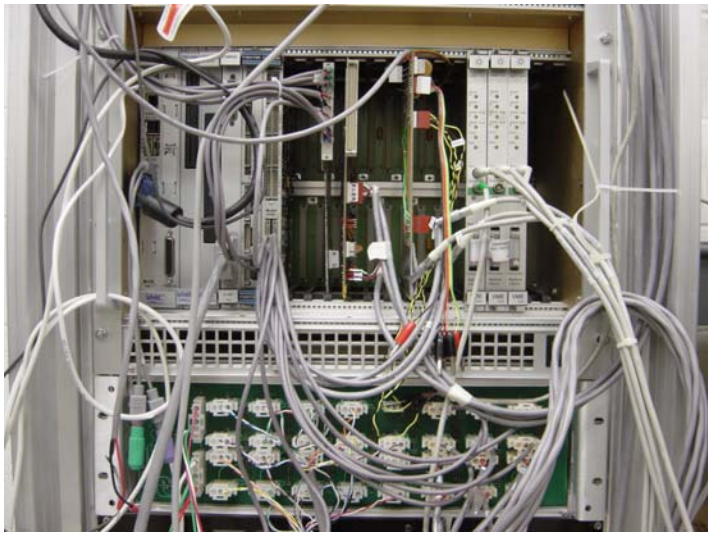

(c)

Figure 2-5 (a) Whole VME system, (b) ADE 3800 boards and power supplies, and (c) VME 7751 VME PC, Pentek DSP board, Pentek 6102 data acquisition board, VME chassis, Agilent 10897B laser axis boards, and power amplifier

2.3.1 Sensors

In order to achieve precision real-time control, accurate displacement and velocity measurement is required. The three laser interferometers sense the platen motion in the horizontal plane (x-, y-translation and ϕ-rotation). The vertical displacements are sensed by three laser distance sensors (Nanogage 100).

Laser Interferometry

The laser interferometer system shown in Figure 2-6 comprises a laser head, three laser interferometers, beam benders, beam splitters, receivers, plane mirrors and laser-axis board the laser interferometer system. The platen position and velocity data are measured in 3-DOF (translation motions in x and y, rotation motion around z-axis) from these three laser interferometers. The laser head shown in Figure 2-7 (a) has a HeNe laser source at the wavelength of 632.99 nm (Aglient 5517D). The laser beam is separated in three using three beam splitters. The laser-axis board (Agilent 10897B) has 0.6-nm position resolution. The laser-axis boards give 35-bit-displacement and 24-bit-velocity.

Laser Distance Sensor

Vertical positions (x- and y-rotation motion, and z-translation) are detected by laser distance sensors (Nanogage 100) shown in Figure 2-8. They have a 100-μm measurement range, 15-nm sensing resolution, and 100-kHz bandwidth. Three channels of 16-bit analog-to-digital converters (ADCs) (Pentek 6102) are used for data acquisition. The input and output voltage swings are ±5 V and ±10 V, respectively.

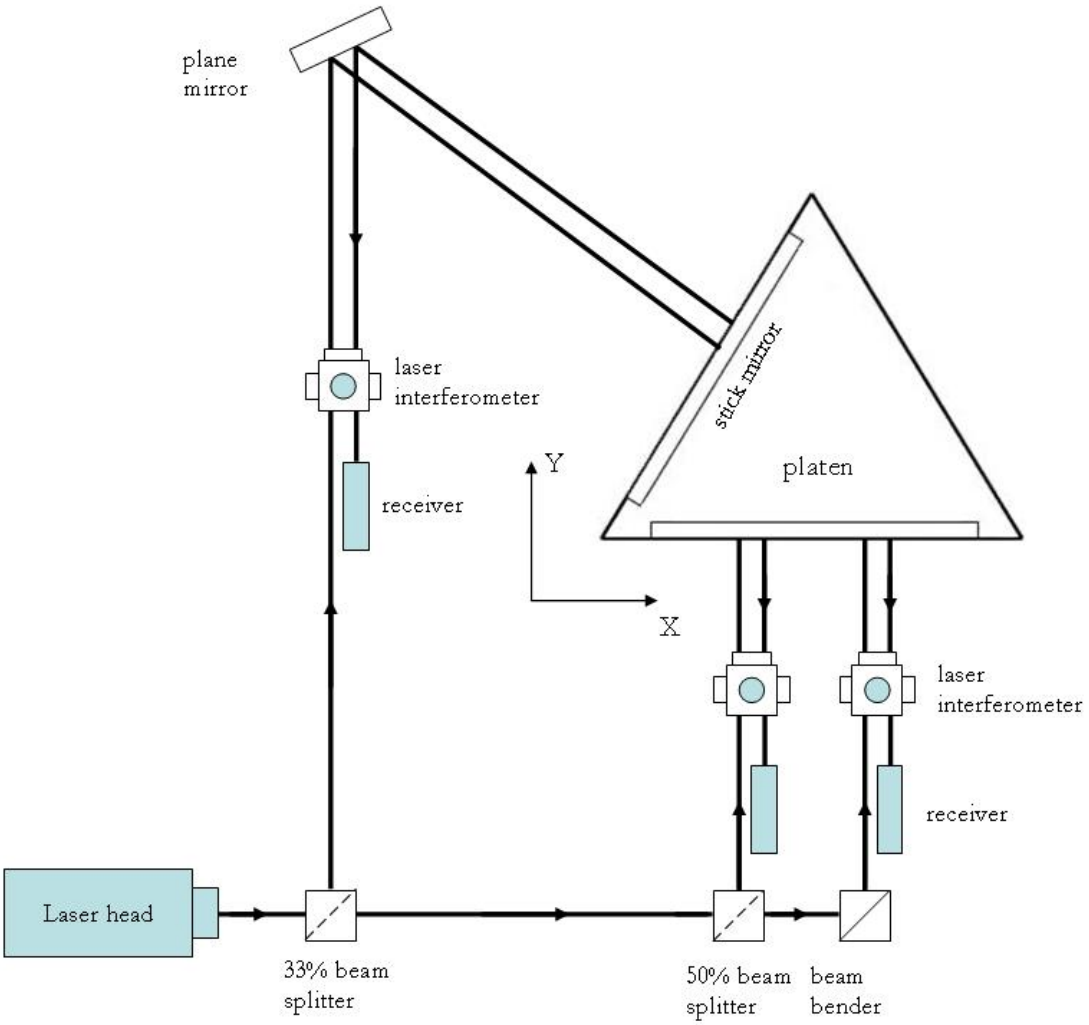

Figure 2-6 Laser interferometer setup

(a) (b)

Figure 2-7 (a) Laser head (HP 5517D), and (b) Laser interferometer and mount (Agilent 10706B)

(a)

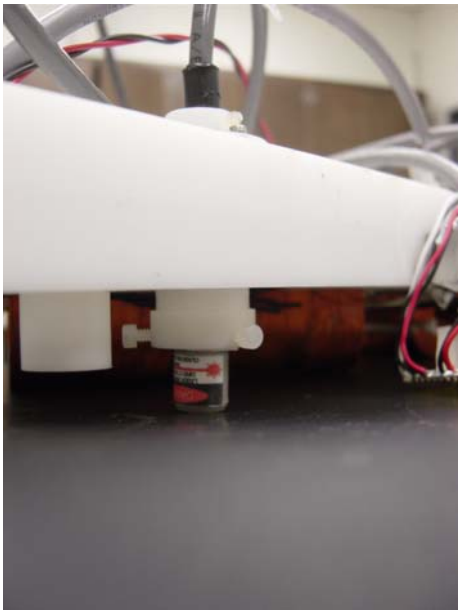

(b) (c)

Figure 2-8 (a) Nanogage 100 laser distance sensor, (b) side view of the vertical sensor mount, and (c) bottom view of the vertical sensor mount

2.3.2 Digital Signal Processor

The Pentek 4284 digital signal processor board contains a TMS320C40 DSP by Texas instruments with 50 million-floating-point operations per second (MFLOPS) computational capability. A Pentek 4284 DSP board works on a VMEbus as a contoller. The laser-axis boards and the data-acquisition board send the real-time sensor data to the DSP, and the DSP sends output commands to the 12-bit digital-to-analog converter (DAC) board (DATEL DVME622).

2.4 Control Structure

The control structure depicted in Figure 2-9 shows the signal and data flows for the 6-DOF precision positioner. Position and velocity information and control outputs are processed in a ISR. The DSP board runs at a sampling frequency of 5 kHz.

Control Software

We use a VME PC (VMIC 7751) with a Pentium III 733-MHz processor and 256 MB RAM [16]. There are several commercial software packages we use in order to control the 6-DOF precision positioner, such as Swiftnet, Code Composer, and Visual C++. The Swiftnet acts as a control panel communication and data interaction between the VME PC and the DSP board. This runs whenever the DSP is operational. The Code Composer (by Texas Instrument) compiles the projects and makes the code run on the DSP.

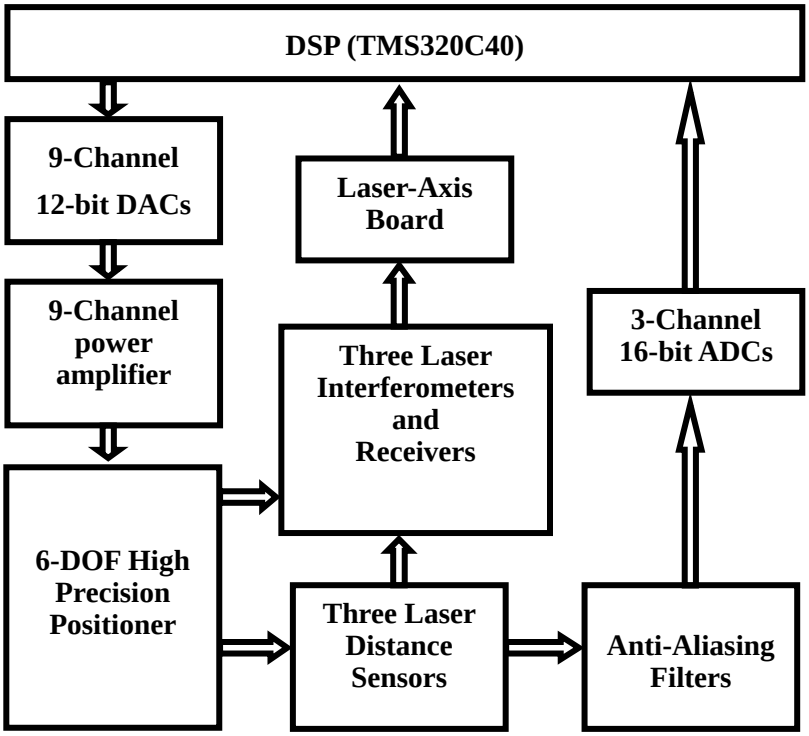

Figure 2-9 Schematic diagram of the control structure

CHAPTER III

DYNAMIC MODELING

With the mass and inertia tensor of the platen and the resistance and inductance of the phase winding, the dynamic model of the platen is derived in this chapter. The specifications of the levitation system are also given. Eventually linearlized state-space models for vertical and lateral motions are derived.

3.1 Mass and Inertia Tensor of the Platen

The total mass of the platen is M = 5.91 kg, so its weight is 57.98 N that includes the Derlin triangular frame, three planar-motor windings, two stick mirrors, three air-bearing assemblies, and three vertical sensors. The vertical force generated by the 3 levitation motors is 68.6 N so that it can be fully levitated. The moments of inertia are calculated about the platen center of mass

$$I = \begin{bmatrix} I_{xx} & -I_{xy} & -I_{xz} \\ -I_{yx} & I_{yy} & -I_{yz} \\ -I_{zx} & -I_{zy} & I_{zz} \end{bmatrix} = \begin{bmatrix} 0.0357 & -0.00120 & -0.000808 \\ -0.00120 & 0.0261 & 0.000263 \\ -0.000808 & 0.000263 & 0.0561 \end{bmatrix} \quad (3.1)$$

in the unit of kg•m². The products of inertia, $I_{xy}, I_{xz}, I_{yx}, I_{yz}, I_{zx}$, and I_{zy} are neglected in the derivation of the dynamic model because any of them is less than 5% of the principal moments of inertia.

3.2 Specification of the Positioner

Specification of the positioner is showed in this section.

- Number of phases, q = 3
- Phase inductance = 15.264 mH
- Phase resistance = 19.44 Ω
- Nominal phase current = 0.56 A
- Maximum phase current = 1.26 A
- Nominal phase voltage = 11.6 V
- Maximum phase voltage = 26.1 V

Parameters of the magnet arrays and windings are:

- Turn density, η_0 = 3.5246 × 10^6 turns/m²
- Pitch, l = 50.977 mm = 2.007”
- Magnet matrix size : 304.8 mm × 304.8 mm
- Number of magnet pitches, N_m = 2
- Magnet thickness, $\Delta = l/4$
- Winding thickness, $\Gamma = l/5$
- Magnet remanence, $B_r = \mu_0 M_0$ = 1.43 T
- Nominal peak current density, $J_p = 2 \times 10^6$ A/m²

The motion capabilities of the maglev positioner are:

- Planar travel range = 120 mm × 120 mm
- Nominal motor air gap = 2.3 mm
- Vertical range = 100 μm
- Maximum velocity = 24.8 mm/s

3.3 Decoupled Equations of Motion

The linearlized force equations and vertical and lateral linear equations of motions are derived in this section.

3.3.1 *DQ* Decomposition

Both the direct-axis (*D*-axis) and the quadrature-axis (*Q*-axis) are attached to the mover so that these two axes move together with the platen. Therefore there is no dependence in the force equations with respect to the stator which is magnet matrix in the *DQ* frame. The nonlinear term can be eliminated. The *D*-axis is parallel to the stator magnetic axis and the *Q*-axis is perpendicular with *D*-axis shown as Figure 3-1. The vertical motion is affected by the *D*-component current, and the horizontal driving forces are affected by the *Q*-component current. In order to control the two-DOF suspension and the driving force, the planar motor requires the decoupled two orthogonal force components.

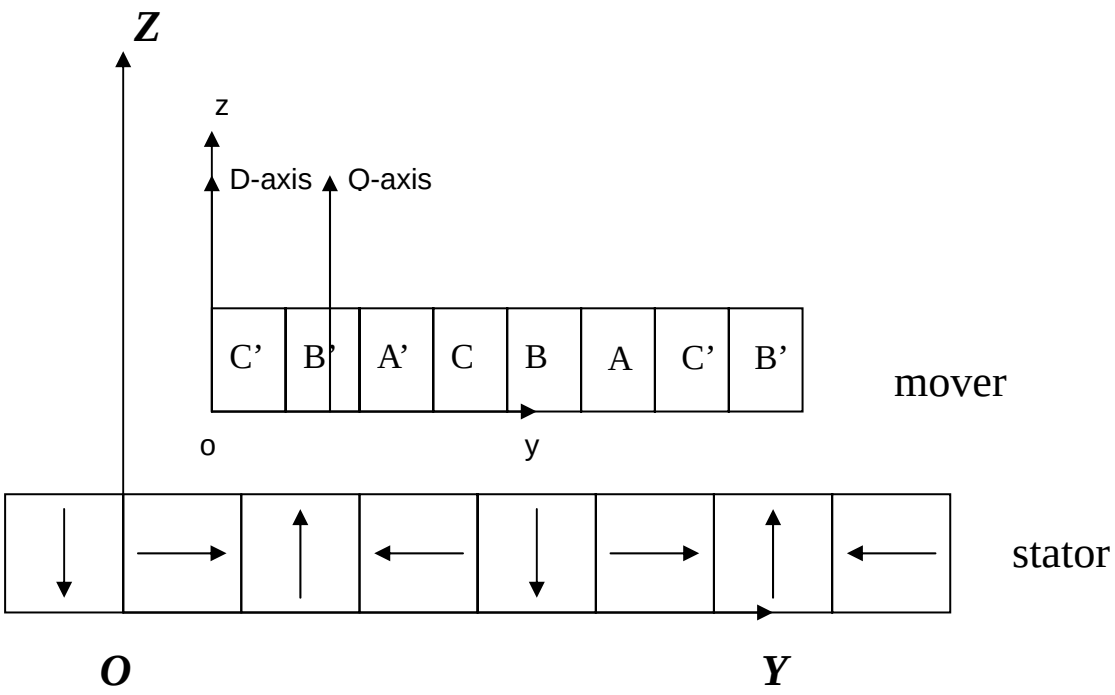

Figure 3-1 *DQ* coordinates attached to the platen [7]

3.3.2 Linearized Force Equations

The following equation shows the force generated by one pitch of the levitation motor [7],

$$\begin{bmatrix} f_y \\ f_z \end{bmatrix} = \frac{1}{2}\mu_0 M_0 \eta_0 N_m G e^{-\gamma_1 z_0} \begin{bmatrix} \cos\gamma_1 y_0 & \sin\gamma_1 y_0 \\ -\sin\gamma_1 y_0 & \cos\gamma_1 y_0 \end{bmatrix} \begin{bmatrix} i_a \\ i_b \end{bmatrix} \tag{3.2}$$

where the f_y is *y*-directed and f_z is *z*-directed forces, respectively, and the constant *G* is following.

$$G = \frac{\sqrt{2} w l^2}{\pi^2}(1 - e^{-\gamma_1 \Gamma})(1 - e^{-\gamma_1 \Delta}), \tag{3.3}$$

This contains the effects of the motor geometry, which has the value of $1.072 \times 10^{-5} m^3$. Here i_a and i_b represent the peak current components. y_0 is the horizontal relative displacements of

the motors *A* and *B* from the initial position. The other parameters are as follows; magnet remanence is $\mu_0 M_0$ = 0.71 T, winding turn density is η_0 = 3.5246×10^6 turn/m², effective spatial period is N_m = 2, and absolute value of fundamental wave number is γ_1 = $2\pi / l$ = $123.25\, m^{-1}$. If the variable y_0 changes to x_0, the same force equation is applied in motor *C*.

3.3.3 Vertical Equations of Motion

The vertical equation of motion is represented as follows,

$$f_z - Mg = 3 \cdot \frac{1}{2} \mu_0 M_0 \eta_0 N_m G(e^{-\gamma_1 z_0} i_D - \gamma_1 e^{-\gamma_1 z_0} i_D z_0 + e^{-\gamma_1 z_0} i_D) \tag{3.4}$$

The factor of three is multiplied because there are 3 planar motors. Equation (3.5) is showed with replacing the weight Mg to $3 \cdot \frac{1}{2} \mu_0 M_0 \eta_0 N_m G e^{-\gamma_1 z_0} i_D$, where the platen achieves a dynamic equilibrium. As a result, the force equation is,

$$f_z = 3 \cdot \frac{1}{2} \mu_0 M_0 \eta_0 N_m G e^{-\gamma_1 z_0} i_D - 3 \cdot \frac{1}{2} \mu_0 M_0 \eta_0 N_m G \lambda_1 e^{-\gamma_1 z_0} i_D z_0 \tag{3.5}$$

and the incremental equation of motion is,

$$M \frac{d^2 z_0}{dt^2} + \mu_0 M_0 \eta_0 N_m G e^{-\gamma_1 z_0} i_D z_0 = 3 \cdot \frac{1}{2} \mu_0 M_0 \eta_0 N_m G \lambda_1 e^{-\gamma_1 z_0} i_D . \tag{3.6}$$

3.3.4 Lateral Equations of Motion

The equilibrium condition for the lateral direction comes from (3.2). The force equation in *x*-axis is,

$$f_x = \frac{1}{2} \mu_0 M_0 \eta_0 N_m G e^{-\gamma_1 z_0} (\cos(\gamma_1 y_0) i_a + \sin(\gamma_1 y_0) i_b) \tag{3.7}$$

The force equation in *y*-axis is,

$$f_y = 2 \cdot \frac{1}{2} \mu_0 M_0 \eta_0 N_m G e^{-\gamma_1 z_0} (\cos(\gamma_1 y_0) i_a + \sin(\gamma_1 y_0) i_b) . \tag{3.8}$$

Because two planar motors generate *y*-directional force, the factor of two is multiplied. The incremental equation of motion is showed as followed,

$$M \frac{d^2 y_0}{dt^2} + \mu_0 M_0 \eta_0 N_m G e^{-\gamma_1 z_0} i_D y_0 = 2 \cdot \frac{1}{2} \mu_0 M_0 \eta_0 N_m G \gamma_1 e^{-\gamma_1 z_0} i_Q . \tag{3.9}$$

3.4 Dynamic Model of System

As preceding procedures, the linearized equations of motions are derived. We regard the model of platen as a pure mass without any friction.

3.4.1 Linearized Equations of Motion in Horizontal and Vertical Modes

The platen is modeled as a pure mass without friction in full levitation. The following equations represent the dynamics of the pure mass model.

$$M \frac{d^2 x}{dt^2} = f_x \tag{3.10}$$

$$f_x = f_{Cx} , \tag{3.11}$$

The mass of platen is M = 5.91 kg, and f_x is the magnetic modal force generated by motor *C* in Figure 3-2. Table 3-1 shows 6-DOF motions generated by the linear motors. The *x*-direction force is generated by one motor.

$$M \frac{d^2 y}{dt^2} = f_y \tag{3.12}$$

$$f_y = f_{Ay} + f_{By} \tag{3.13}$$

where f_y is the *y*-directional magnetic modal force generated by motors *A* and *B*.

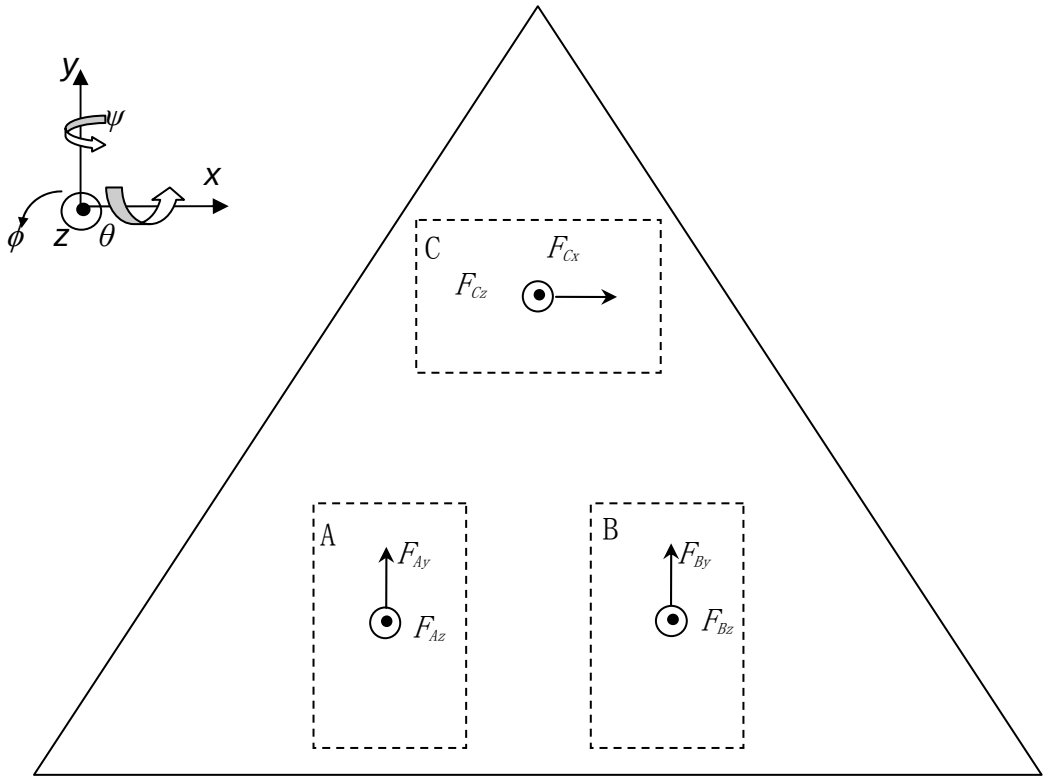

Figure 3-2 Individual force components generated by motors *A*, *B*, and *C* [1]

Table 3-1 6-DOF motions generated by the linear motors [1]

	Motor A	Motor B	Motor C
Δx	$-F_{Ay}$	F_{By}	F_{Cx}
Δy	F_{Ay}	F_{By}	0
Δz	F_{Az}	F_{Bz}	F_{Cz}
$\Delta\phi$	$-F_{Ay}$	F_{By}	0
$\Delta\theta$	$-F_{Az}$	$-F_{Bz}$	F_{Cz}
$\Delta\psi$	F_{Az}	$-F_{Bz}$	0

In order to control rotation motion around the *z*-axis, the following differential equations are used.

$$I_{zz}\frac{d^2\phi}{dt^2} = \tau_z, \tag{3.14}$$

$$\tau = -f_{Ax}l_{Ay} + f_{By}l_{Bx} - f_{Cx}l_{Cy}, \tag{3.15}$$

where the principle moment of inertia for rotation about the *z*-axis is I_{zz} = 0.054 kg•m², and τ_z is a torque generated by the interaction of motors *A*, *B*, and *C* from the magnetic origin about the *z*-axis. The state-space model in the horizontal mode is as follows.

$$\begin{bmatrix} \dot{x} \\ \dot{y} \\ \dot{\phi} \\ \dot{h} \\ \dot{u} \\ \dot{v} \end{bmatrix} = \begin{bmatrix} 0 & 0 & 0 & 1 & 0 & 0 \\ 0 & 0 & 0 & 0 & 1 & 0 \\ 0 & 0 & 0 & 0 & 0 & 1 \\ 0 & 0 & 0 & 0 & 0 & 0 \\ 0 & 0 & 0 & 0 & 0 & 0 \\ 0 & 0 & 0 & 0 & 0 & 0 \end{bmatrix} \begin{bmatrix} x \\ y \\ \phi \\ h \\ u \\ v \end{bmatrix} + \begin{bmatrix} 0 & 0 & 0 \\ 0 & 0 & 0 \\ 0 & 0 & 0 \\ 0 & 0 & \frac{c}{m} \\ \frac{c}{m} & \frac{c}{m} & 0 \\ -\frac{c}{I_{zz}}l_{Az} & \frac{c}{I_{zz}}l_{Bz} & -\frac{c}{I_{zz}}l_{Cy} \end{bmatrix} \begin{bmatrix} i_{Aq} \\ i_{Bq} \\ i_{Cq} \end{bmatrix} \tag{3.16}$$

$$y = \begin{bmatrix} x & y & \phi & h & u & v \end{bmatrix}^T \tag{3.17}$$

The vertical motion equations represent as follows, the vertical directional controller is designed as a spring-mass system in *z* because the platen is levitated by three levitation motors.

$$M\frac{d^2z}{dt^2} = f_z - K_z z \tag{3.18}$$

$$f_z = f_{Az} + f_{Bz} + f_{Cz} \tag{3.19}$$

K_z is the effective spring constant of the levitation motor derived by experiments based on Hooke's law. The following chapter shows the value of K_z. f_z is the vertical directional force, generated by three motors in the same time in order to lift the platen up.

Because of the three magnetic springs in the three levitation motors, the dynamics in the rotation around the *x*- and *y*-axes is regarded as a spring-mass system as follows,

$$I_{xx}\frac{d^2\theta}{dt^2} = \tau_\theta - K_\theta\theta \tag{3.20}$$

$$\tau_\theta = -f_{Az}l_{Ay} - f_{Bz}l_{By} + f_{Cz}l_{Cy} \tag{3.21}$$

$$I_{yy}\frac{d^2\varphi}{dt^2} = \tau_\varphi - K_\varphi\varphi \tag{3.22}$$

$$\tau_\varphi = -f_{Az}l_{Ax} - f_{Bz}l_{Bx} + f_{Cz}l_{Cx} \tag{3.23}$$

where τ_θ and τ_ψ are the torque around the *x*- and *y*-axes respectively. K_θ and K_ψ are the effective torsional spring constants about the *x*- and *y*-axes determined by experiments. The principle moments of inertia are I_{xx} = 0.033 kg•m² and I_{yy} = 0.025 kg•m² in the *x*- and *y*-axes respectively. The state-space model of the vertical mode is as follows.

$$\begin{bmatrix} \dot{z} \\ \dot{\theta} \\ \dot{\varphi} \\ \dot{p} \\ \dot{q} \\ \dot{w} \end{bmatrix} = \begin{bmatrix} 0 & 0 & 0 & 1 & 0 & 0 \\ 0 & 0 & 0 & 0 & 1 & 0 \\ 0 & 0 & 0 & 0 & 0 & 1 \\ -\frac{K_z}{m} & 0 & 0 & 0 & 0 & 0 \\ 0 & -\frac{K_\theta}{I_{xx}} & 0 & 0 & 0 & 0 \\ 0 & 0 & -\frac{K_\varphi}{I_{yy}} & 0 & 0 & 0 \end{bmatrix} \begin{bmatrix} z \\ \theta \\ \varphi \\ p \\ q \\ w \end{bmatrix} + \begin{bmatrix} 0 & 0 & 0 \\ 0 & 0 & 0 \\ 0 & 0 & 0 \\ \frac{c}{m} & \frac{c}{m} & \frac{c}{m} \\ -\frac{c}{I_{xx}}l_{Ay} & -\frac{c}{I_{xx}}l_{By} & \frac{c}{I_{xx}}l_{Cy} \\ \frac{c}{I_{yy}}l_{Ax} & -\frac{c}{I_{Bx}} & -\frac{c}{I_{yy}}l_{Cx} \end{bmatrix} \begin{bmatrix} i_{Ad} \\ i_{Bd} \\ i_{Cd} \end{bmatrix} \tag{3.24}$$

$$y = \begin{bmatrix} I_{3\times3} & 0_{3\times3} \end{bmatrix} \begin{bmatrix} z & \theta & \varphi & p & q & w \end{bmatrix}^T \tag{3.25}$$

3.4.2 Sensor Equation

The three laser interferometers are able to measure the distance and the velocity between the sensors and the stick mirrors. The distance means the *x*-, *y*- and ϕ-motion which move in

horizontal mode. It can be converted by using mathematical method to the coordinates of the positioner.

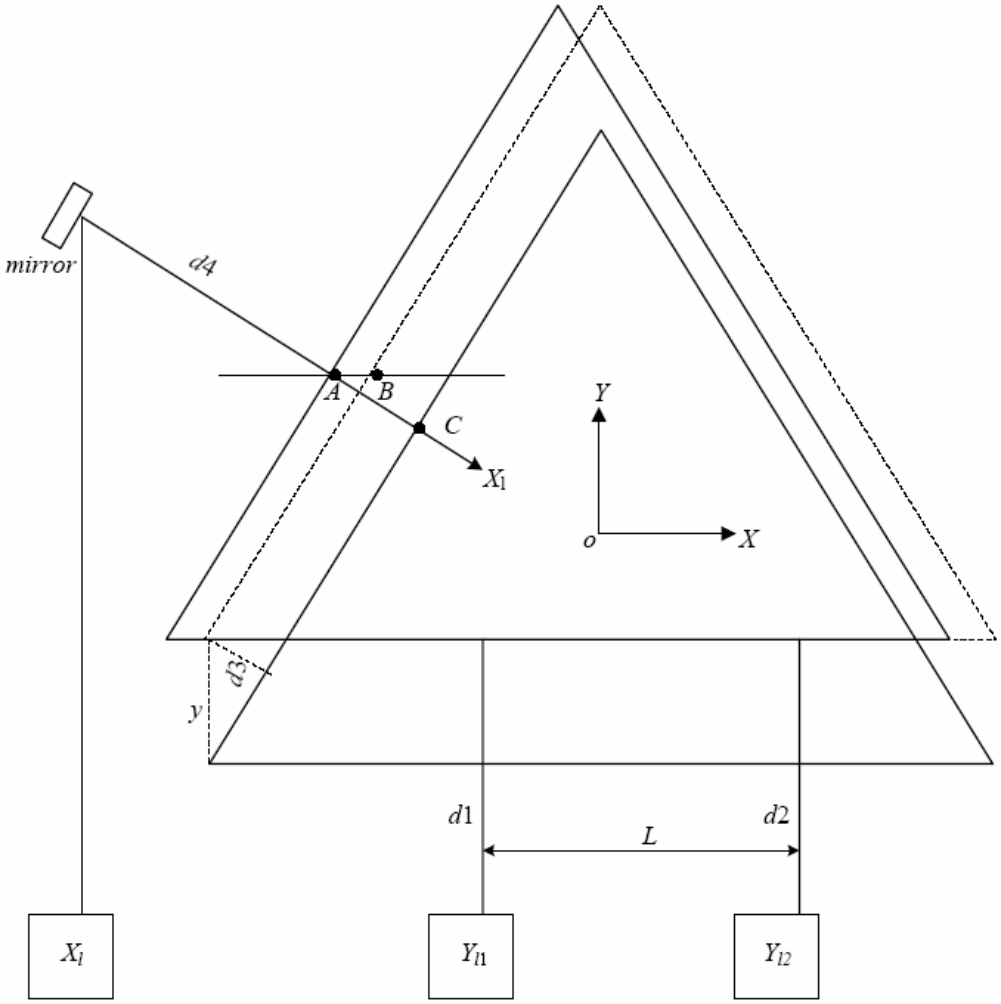

Figure 3-3 Schematic diagram of laser interferometers [1]

Figure 3-3 shows the schematic view and principle of laser interferometer sensors. The laser interferometers Y_{l1} and Y_{l2} can measure the distance in the *y*-direction and rotation motion, ϕ in the z-direction. And sensor X_l can measure the distance in *x*-direction.

$$Y_{l1} = d1 \tag{3.26}$$

$$Y_{l2} = d2 - d1 \tag{3.27}$$

$$X_1 = d4 \tag{3.28}$$

The Y_{l1} represents the distance $d1$ and Y_{l2} means the difference between $d1$ and $d2$. X_l shows the distance between the mirror and platen. By the programming, all laser interferometers are set to be zero in the initial position, which means all of the motions are measured by relative position. The rotation motion angle is obtained as follows.

$$y = Y_{l1} \tag{3.29}$$

$$\tan\phi = \frac{d2 - d1}{L} = \frac{Y_{l2}}{L} \tag{3.30}$$

$$\phi = \frac{Y_{l2}}{L} \tag{3.31}$$

$$x = -l_{BA} = \frac{-I_{CA} + d3}{\cos 30^\circ} = \frac{X_l + y\sin 30^\circ}{\cos 30^\circ} \tag{3.32}$$

$$x = \frac{X_l}{\cos 30^\circ} + Y_{l1}\tan 30^\circ \tag{3.33}$$

$$\begin{bmatrix} x \\ y \\ \phi \\ h \\ u \\ v \end{bmatrix} = \begin{bmatrix} \frac{1}{\cos 30^\circ} & \tan 30^\circ & 0 & 0 & 0 & 0 \\ 0 & 1 & 0 & 0 & 0 & 0 \\ 0 & 0 & \frac{1}{L} & 0 & 0 & 0 \\ 0 & 0 & 0 & \frac{1}{\cos 30^\circ} & \tan 30^\circ & 0 \\ 0 & 0 & 0 & 0 & 1 & 0 \\ 0 & 0 & 0 & 0 & 0 & \frac{1}{L} \end{bmatrix} \begin{bmatrix} X_l \\ Y_{l1} \\ Y_{l2} \\ V_l \\ V_{l1} \\ V_{l2} \end{bmatrix} \tag{3.34}$$

The vertical sensor relations are shown as follows.

$$\begin{bmatrix} z_1 \\ z_2 \\ z_3 \end{bmatrix} = \begin{bmatrix} -z_{y1} & -z_{x1} & 1 \\ z_{y2} & -z_{x2} & 1 \\ -z_{y3} & z_{x3} & 1 \end{bmatrix} \begin{bmatrix} \theta \\ \varphi \\ z \end{bmatrix} \tag{3.35}$$

According to geometry values from Figure 3-4 and Table 3-2, following equation (3.36) is obtained by plugging the values in. This is the sensor transformation equation for vertical mode.

$$\begin{bmatrix} \theta \\ \varphi \\ z \end{bmatrix} = \begin{bmatrix} -2.410 & 4.600 & -2.190 \\ -3.946 & 0.127 & 3.818 \\ 0.315 & 0.289 & 0.410 \end{bmatrix} \begin{bmatrix} z_1 \\ z_2 \\ z_3 \end{bmatrix} \tag{3.36}$$

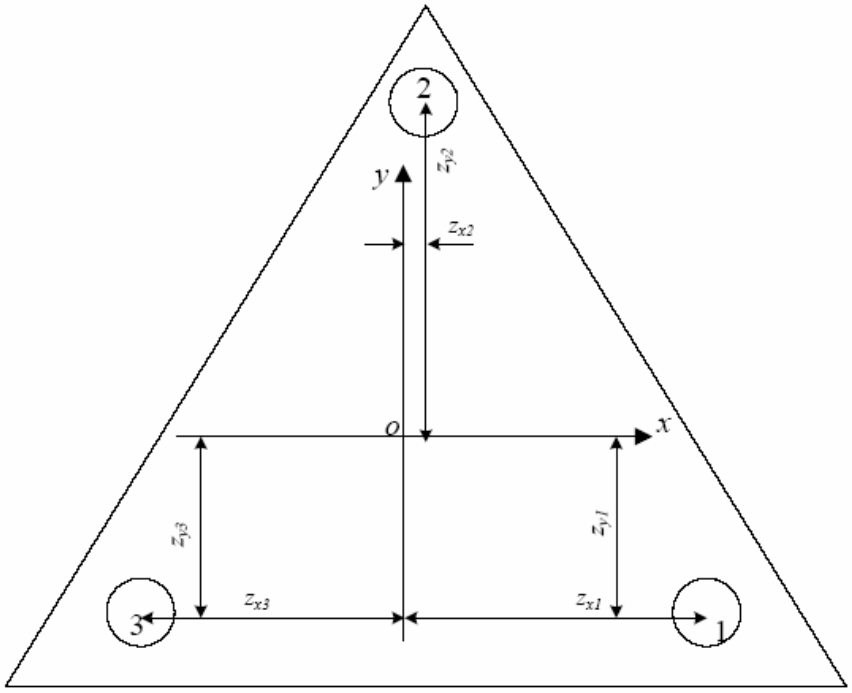

Figure 3-4 Position of laser distance sensors [1]

Table 3-2 Values of length variables in Figure 3-4 [1]

Variable	Value (mm)	Variable	Value (mm)
z_{y1}	58.9	z_{x1}	141.1
z_{y2}	155.1	z_{x2}	18.3
z_{y3}	66.0	z_{x3}	116.7

CHAPTER IV

CONTROLLER DESIGN

4.1 Digital Controller Design Procedure

4.1.1 Controller for Vertical Mode

From Chapter III, the decoupled vertical dynamic equation of motion can be shown as follows,

$$M\frac{d^2z}{dt^2} + 2\mu_0 M_0 \eta_0 N_m G\gamma_1 e^{-\gamma_1 z} i_D z = 2\mu_0 M_0 \eta_0 N_m G e^{-\gamma_1 z} i_D \tag{4.1}$$

By substituting the parameters,

$$5.91\frac{d^2z}{dt^2} + 2382z = f_z\,, \tag{4.2}$$

where f_z is the modal force that is a sum of the decomposed vertical force, and the magnetic spring constant of K = 2382 N/m was determined.

First, the continuous-time controller in the *s*-domain was designed, and then it was converted to a discrete-time controller in the *z*-domain using Matlab SISO tool with the following pole-zero mapping technique [17–18].

$$z = e^{sT} \tag{4.3}$$

The sampling rate is 5 kHz. The delay was neglected because the sampling rate is much higher than the closed-loop control bandwidth.

The following compensator is designed by MATLAB SISO tools and the gain is determined. The damping ratio is ζ = 0.5.

$$G_z(s) = 2300642\left(\frac{s+137.21}{s+1036}\right)\left(\frac{s+10}{s}\right) \tag{4.4}$$

The dominant poles are located at –289 ± *j*192 rad/s. The closed-loop natural frequency is 55.23 rad/s. And then, through the pole-zero mapping technique, the controller was transferred to digital lead-lag compensator as follows,

$$G_z(z) = 2126342\left(\frac{z-0.9754}{z-0.8129}\right)\left(\frac{z-0.998}{z-1}\right) \tag{4.5}$$

The sampling period is 200 μs. The gain of the digital controller was determined by via the SISO tool with respect to the continuous-time controller. Figure 4-1 represents a root locus. A block diagram of the vertical motion controller is given in Figure 4-2 with parameters, A = 0.9754, B = 0.8129, C = 0.998, D = 1, and K = 2126342. Figure 4-3 shows a loop transmission with a resonance peak at 3.18 Hz, and Figure 4-4 is a closed-loop Bode plot. These two graphs are Matlab simulations.

The controller for θ was designed after the control loop for the vertical motion was closed. The closed-loop control bandwidth is set at 40 Hz and the phase margin of 50˚ is considered. The continuous-time controller in θ is shown as follows.

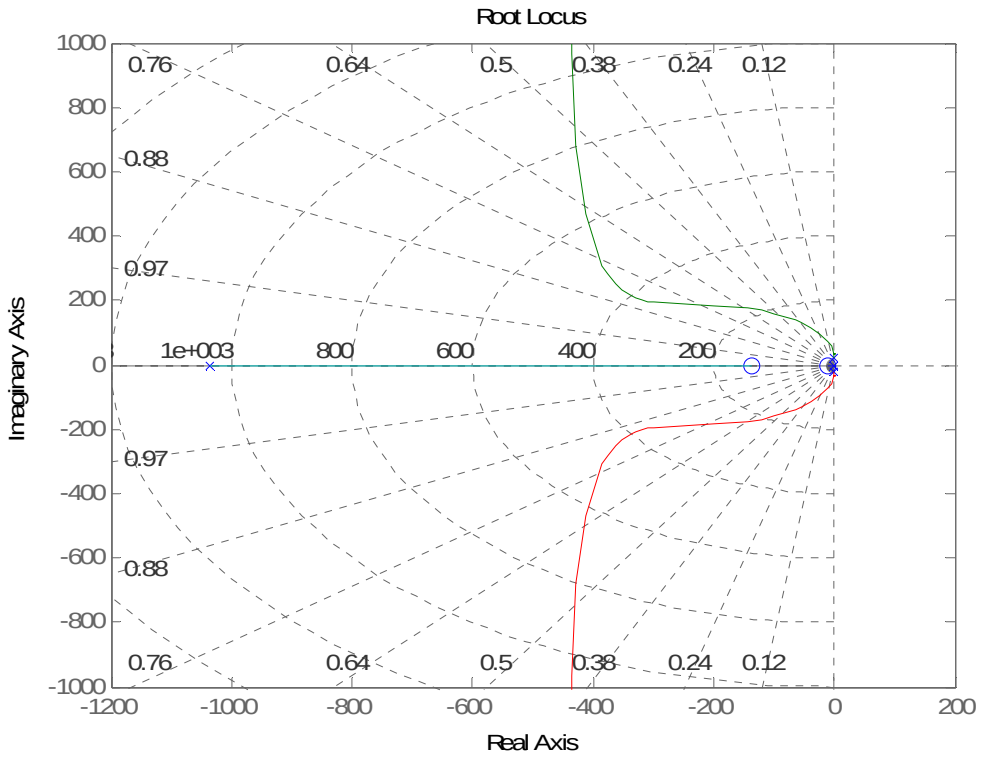

Figure 4-1 Root locus

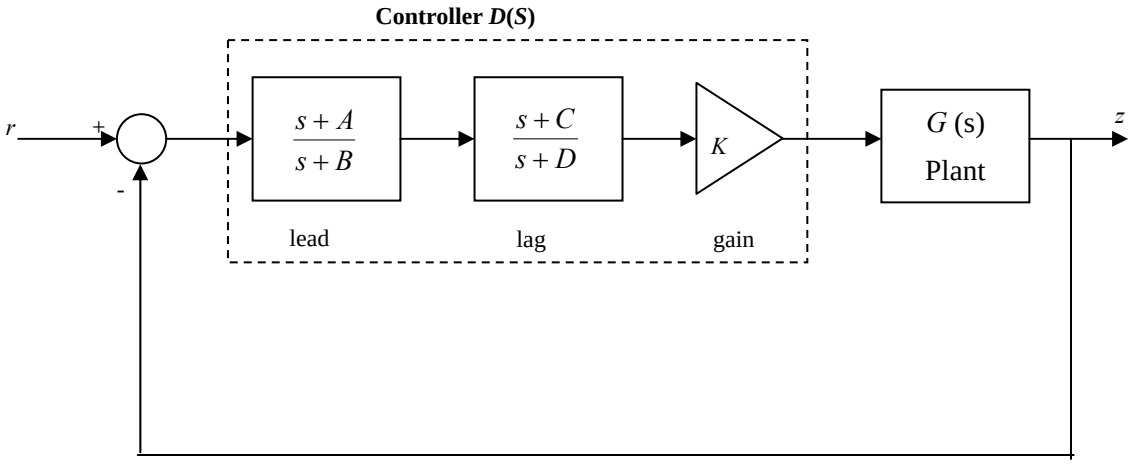

Figure 4-2 Block diagram for the lead-lag controller

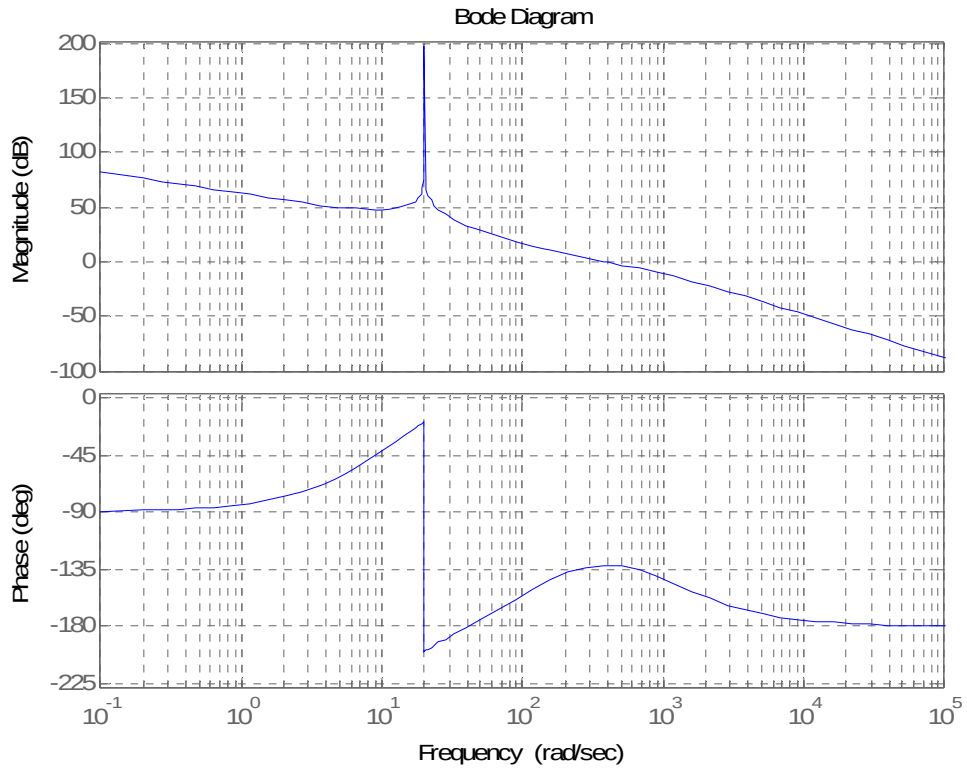

Figure 4-3 Loop transmission for z

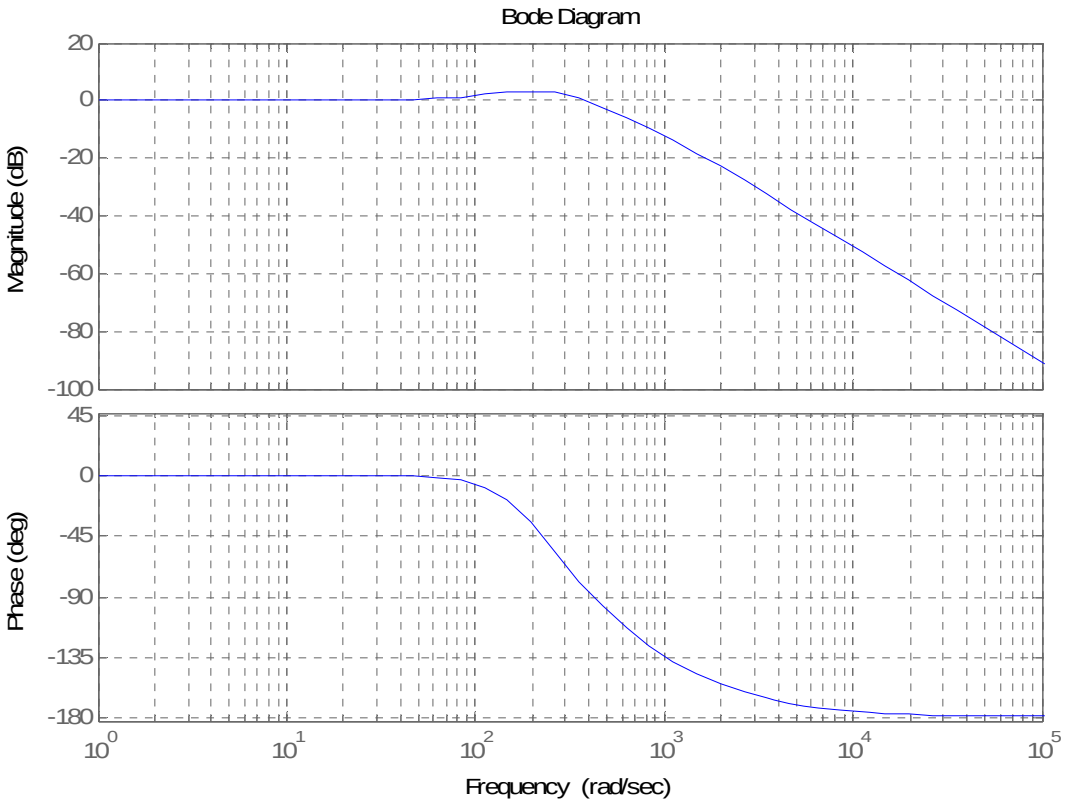

Figure 4-4 Closed-loop Bode plot for *z*

$$G_\theta(s) = 5703\left(\frac{s+91.47}{s+690.5}\right)\left(\frac{s+10}{s}\right). \tag{4.6}$$

The dominant poles are located at –185 ± *j*130 rad/s, and the closed-loop natural frequency is 35.97 Hz. We can get the discrete-time controller via the pole-zero mapping technique with the same sampling frequency. The digital controller in θ is as follows,

$$G_\theta(z) = 5434\left(\frac{z-0.983}{z-0.871}\right)\left(\frac{z-0.998}{z-1}\right) \tag{4.7}$$

Figure 4-5 is a root locus for θ and Figures 4-6 and 4-7 are the loop transmission and closed-loop Bode plot for θ, respectively. Unlike *z* motion, there is no resonance peak in the loop transmission, because the magnetic spring constant is not considered.

Another controller in ψ was also designed with the same method with the different moment of inertia (I_{yy} = 0.025 kg•m²). The closed-loop control bandwidth is set at 40 Hz, and the phase margin is 50˚ with following continuous-time compensator.

$$G_\psi(s) = 4321\left(\frac{s+91.47}{s+690.5}\right)\left(\frac{s+10}{s}\right) \tag{4.8}$$

The dominant poles are located at –185 ± *j*130 rad/s with the closed-loop natural frequency of 226 rad/s. Then, the controller is transferred to a digital lead-lag compensator via the pole-zero mapping technique as follows.

$$G_\psi(z) = 4101\left(\frac{z-0.983}{z-0.871}\right)\left(\frac{z-0.998}{z-1}\right) \tag{4.9}$$

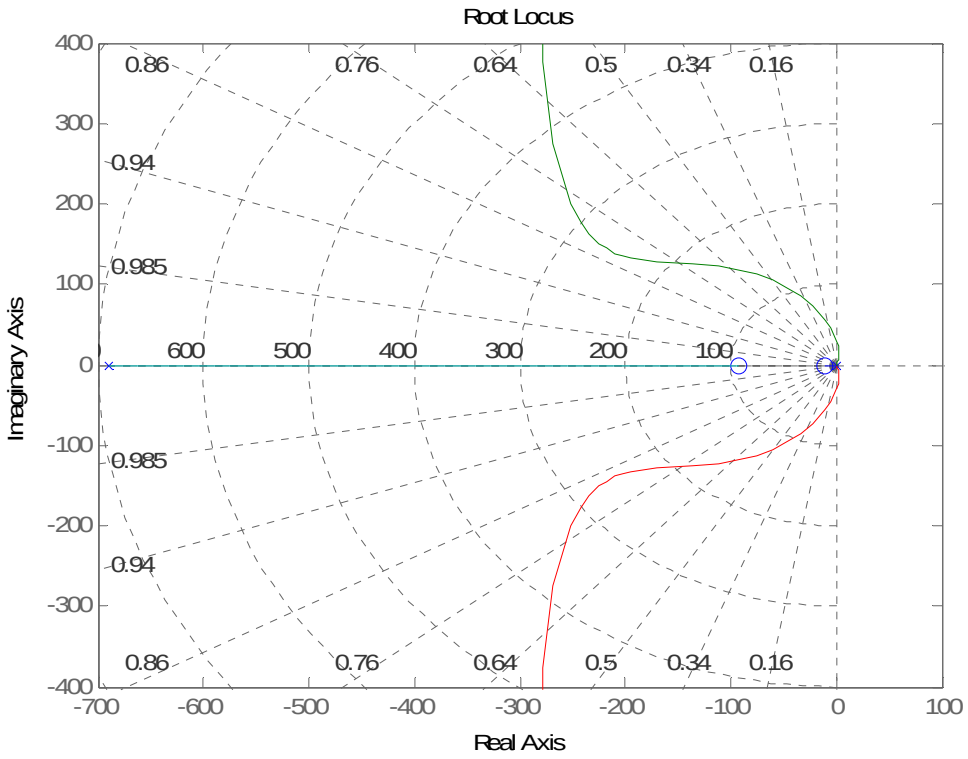

Figure 4-5 Root locus for θ

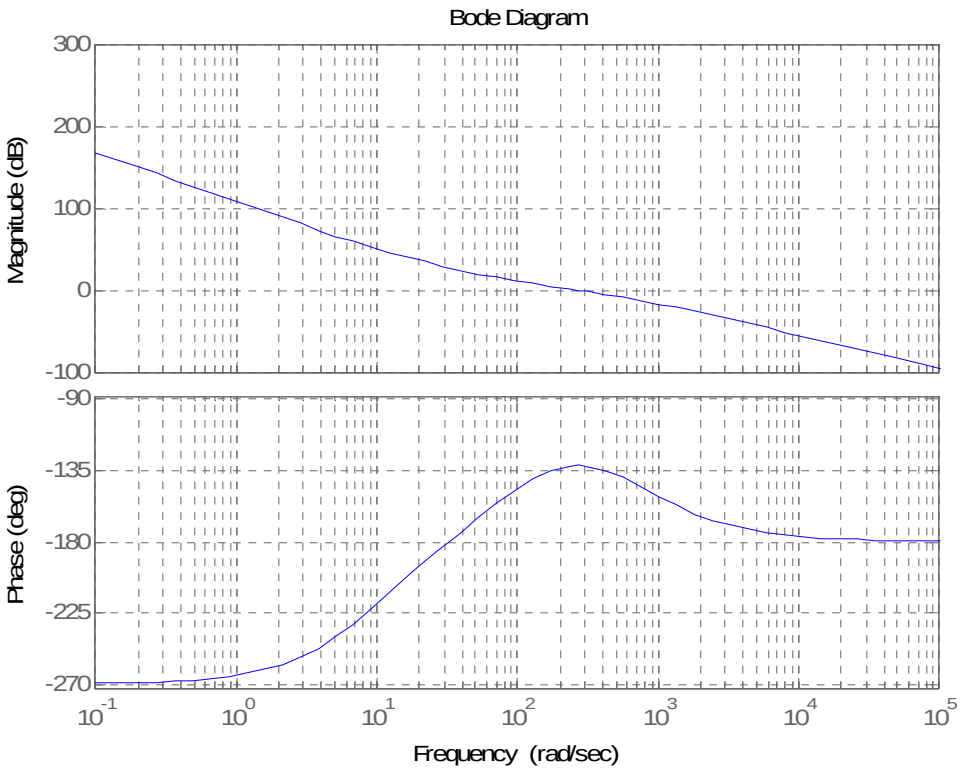

Figure 4-6 Loop transmission for θ

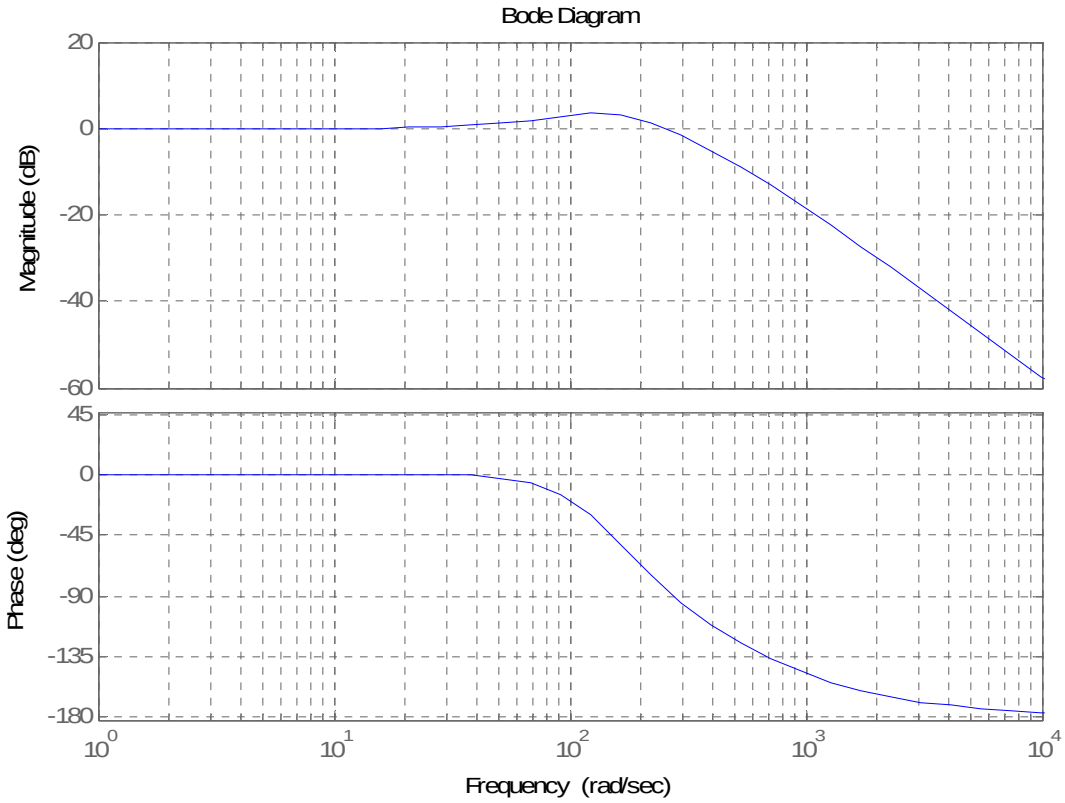

Figure 4-7 Closed-loop Bode plot for θ

4.1.2 Controller for Lateral Mode

As derived in Chapter III, the decoupled lateral translational dynamics is,

$$M\frac{d^2x}{dt^2} - \mu_0 M_0 \eta_0 N_m G e^{-\gamma_1 z} i_D x = \mu_0 M_0 \eta_0 N_m G e^{-\gamma_1 z} i_Q \quad . \tag{4.10}$$

After the nominal and geometric parameters were substituted, this equation became,

$$5.91\frac{d^2x}{dt^2} = f_x, \tag{4.11}$$

where f_x is a modal force, a sum of the decomposed lateral force components. The following digital lead-lag compensator for *x* and *y* was designed with MATLAB SISO tools.

$$G_{x,y}(z) = 74000\left(\frac{z-0.9903}{z-0.7970}\right)\left(\frac{z-0.9979}{z-1}\right) \tag{4.12}$$

The crossover frequency is 21 Hz, and the phase margin is 58˚. The equation below is digital controller for ϕ.

$$G_{\phi}(z) = 13100\left(\frac{z-0.9903}{z-0.7970}\right)\left(\frac{z-0.9979}{z-1}\right) \tag{4.13}$$

The crossover frequency is 38 Hz, and the phase margin is 63˚. Both compensators have a sampling frequency of 5 kHz like those in the vertical mode.

CHAPTER V

6-DOF CLOSED-LOOP EXPERIMENTAL RESULTS

In precision manufacturing, 6-axis fine-motion control is required. In this chapter, several experimental results are given. The generation of micro- and nano-scale stepping motions and large range travel motions is required in semiconductor manufacturing. These results demonstrate the potential utility of the maglev positioner in the precision manufacturing industry.

5.1 Experimental Setup

All 6-DOF motions are tested with the digital controllers implemented. Whereas the previous research by Tiejun Hu a former PhD student of Dr. Won-jong Kim used aerostatic bearings. This research applies the maglev principle. Figure 5-1 shows photographs of the initial setting before magnetic levitation and after magnetic levitation. The 0.04-inch-thick plastic shims were removed at a 70 μm levitated height, and the levitation height was reduced.

Some restrictions exist for initial position setting. As we can see Figure 5-2, the available initial working positions are 2 inches away in both x and y because the magnet matrix and the planar motor have a pitch of 2 inches. Using the permanent marker, The initial position was marked using a permanent marker. Next, the three laser interferometers should be within their active sensing ranges simultaneously, which can be noticed when the green LEDs (light-emitting diodes) on laser receivers are turned on. After the initial positsion setting is made, the platen can perform levitation, stepping motions, or long trajectory scanning motions.

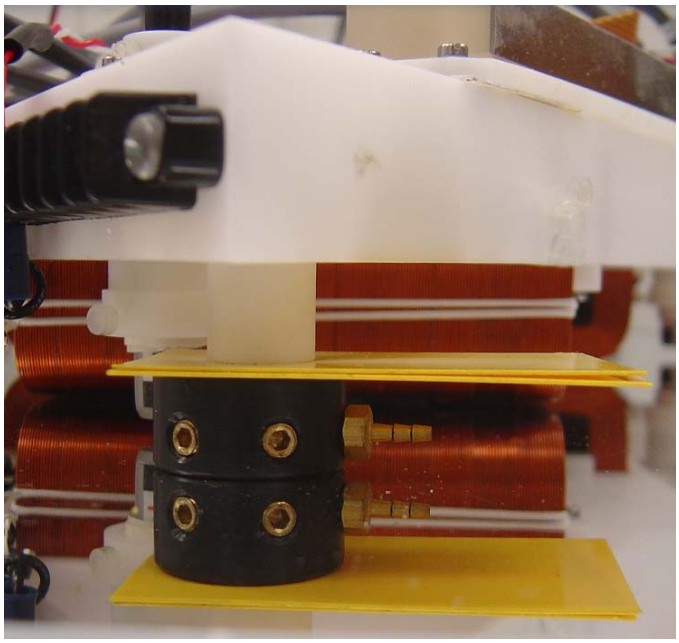

(a)

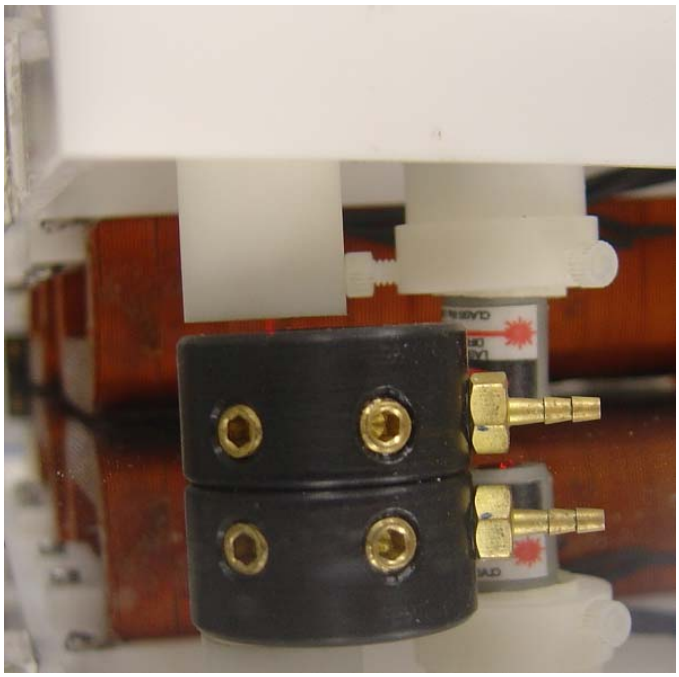

(b)

Figure 5-1 (a) Initial setting with shims of 0.04-inch-thick and (b) after magnetic levitation without shims

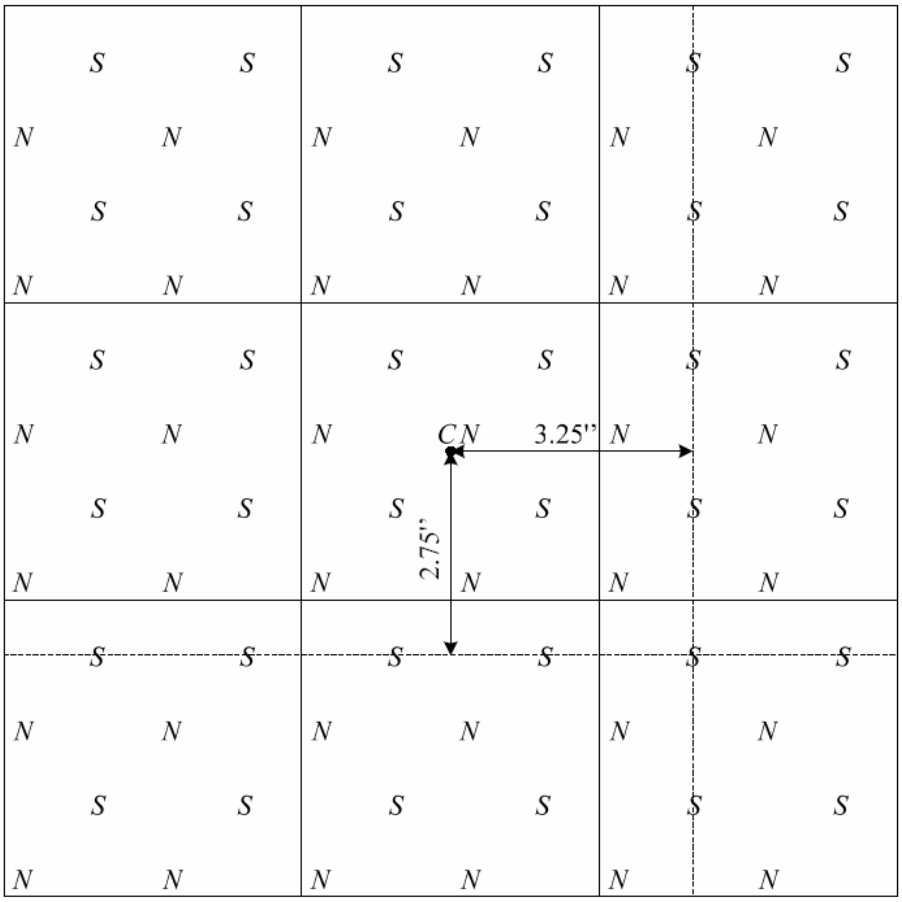

Figure 5-2 Initial position of the positioner [1]

5.2 Step Responses

10-μm, 5-μm, and 30-μm step responses in the *x*-axis with other 5-axis perturbation responses are shown in Figures 5-3–5-5. The plots show that the rise time is less than 3 ms, the settling time is around 100 ms without any steady-state errors in *x*, and the percent overshoot is about 20 %. Unexpected oscillations might occur due to the disturbances originated from the building, the dynamics of the power and sensor cables connected to the VME chassis, although we use a vibration-isolation optical table (Newport RS 3000). The dynamic coupling with other five axes can be one of the reasons for the perturbation. Figures 5-6 and 5-7 show 10-μm and 20-μm step responses in the *y*-axis with perturbation in other 5 axes. It also has 20 % overshoot, 30 ms rise time, and 100 ms settling time. Responses with the step sizes of 5 μm and 10 μm in the *z*-axis are shown in Figures 5-8 and 5-9. The *z*-axis step responses exhibit 30 ms rise time, 20 % overshoot, and less than 100 ms settling time. The 20-μm step responses in θ, φ, and ψ are shown in Figures 5-10, 5-11, and 5-12 respectively.

Figure 5-13 shows the capabilities in nanoscale stepping motion in *x*. There is 60-nm peak-to-peak position noise. The Fast Fourier Transform (FFT) plots indicate that the dominant noise frequency is about 150 Hz.

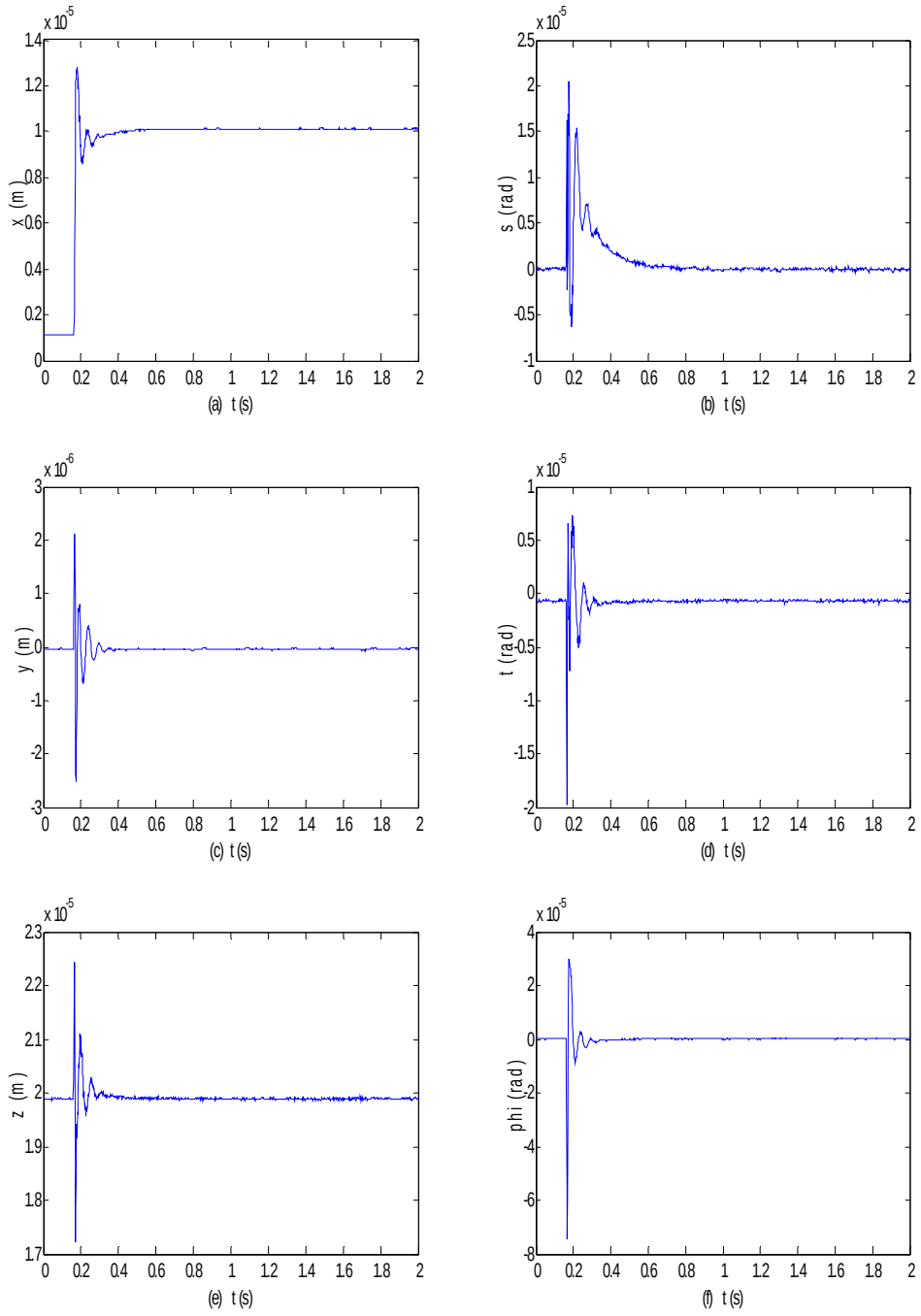

Figure 5-3 10-µm *x*-axis step response at a 20-µm levitation height with perturbations in other axes

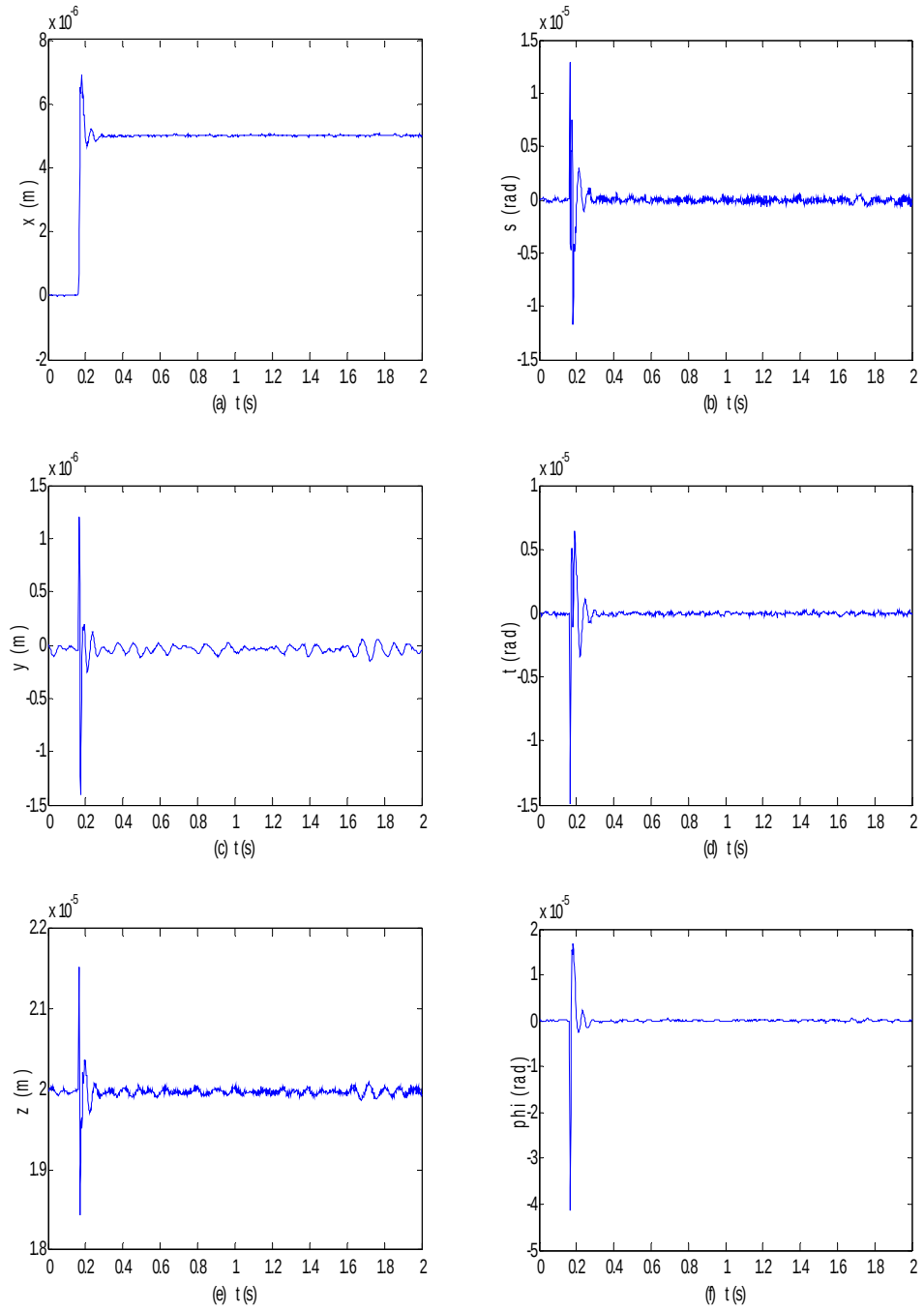

Figure 5-4 5-µm *x*-axis step response at a 20-µm levitation height with perturbations in other axes

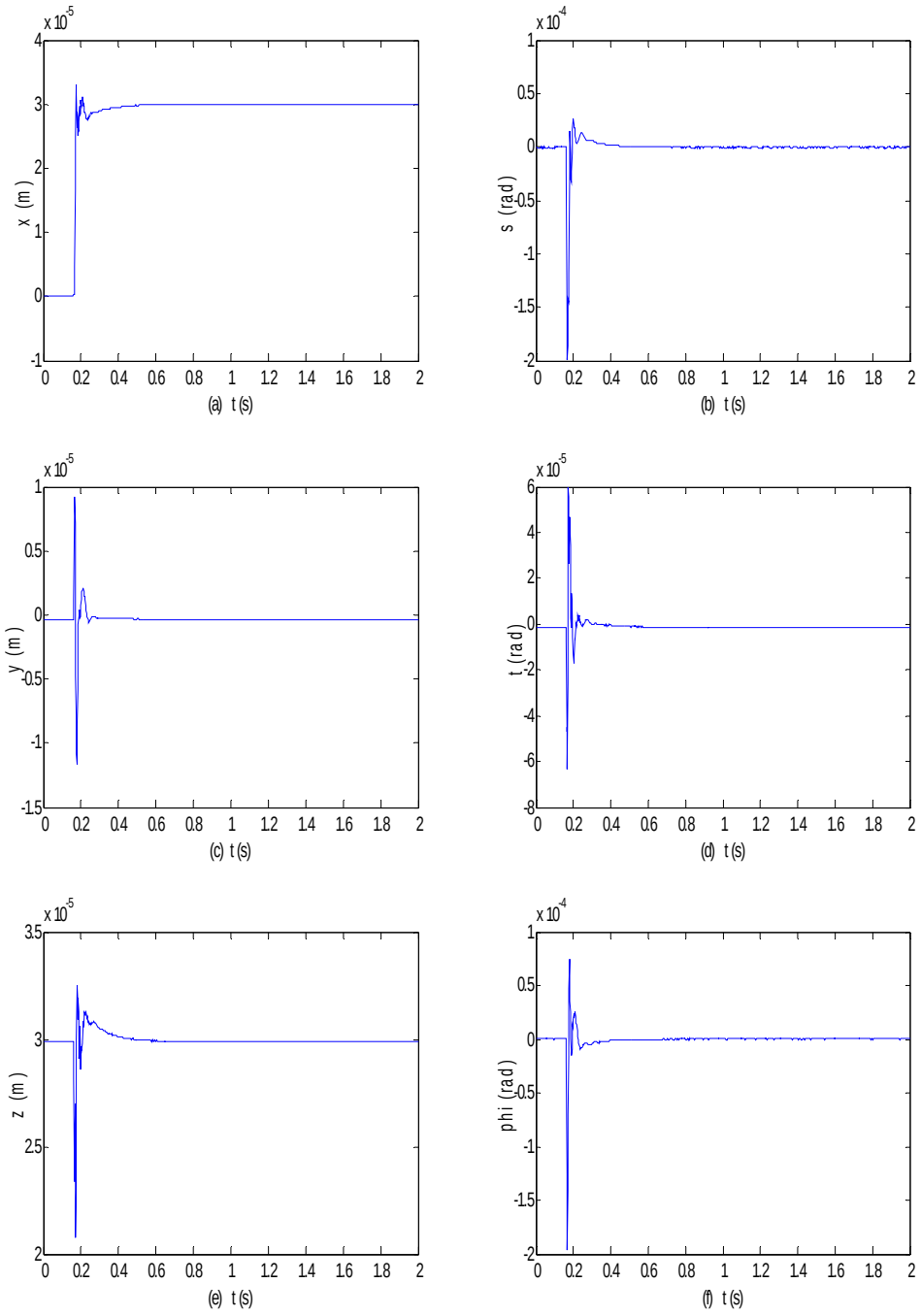

Figure 5-5 30-µm *x*-axis step response at a 30-µm levitation height with perturbations in other axes

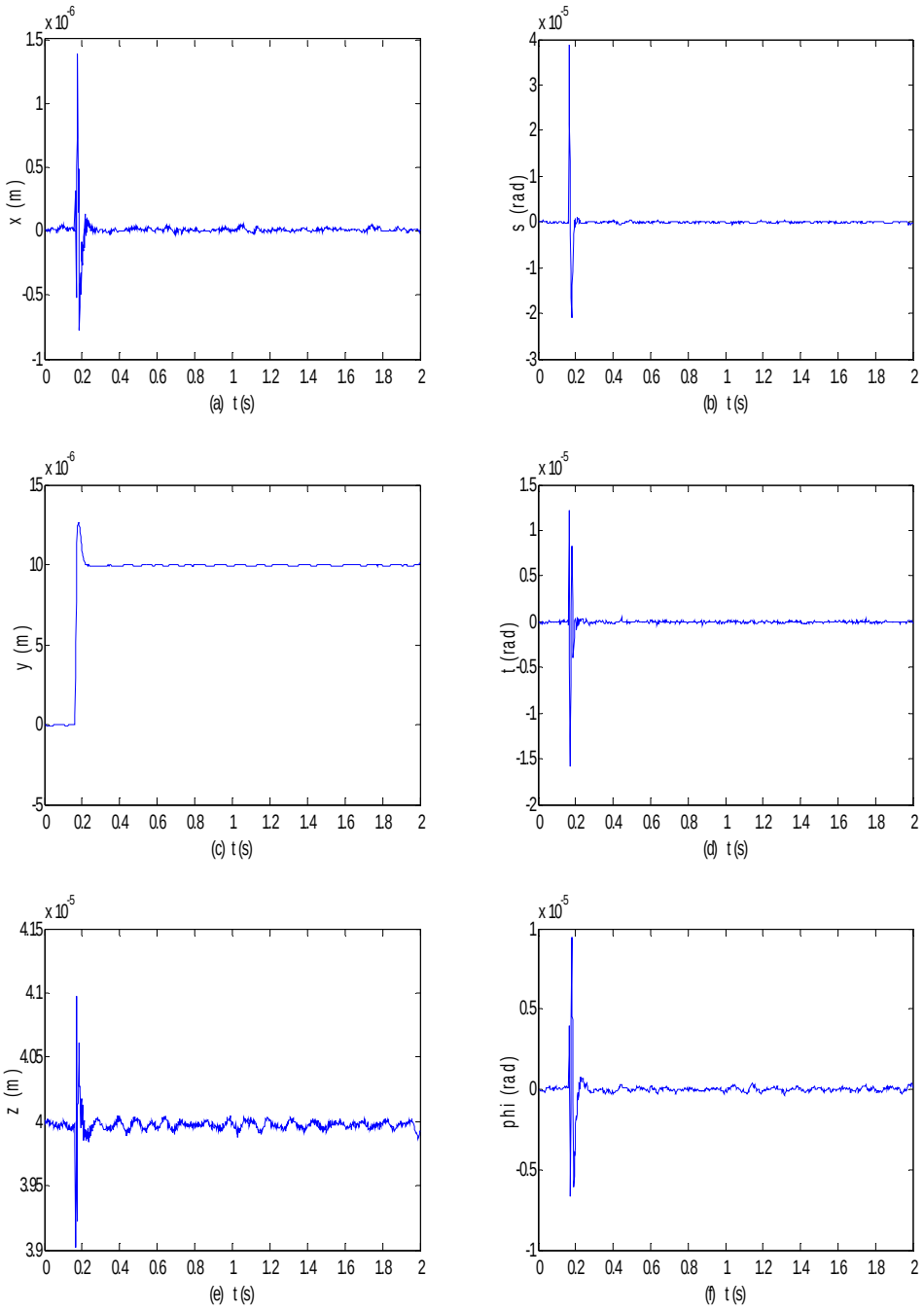

Figure 5-6 10-µm *y*-axis step response at a 40-µm levitation height with perturbations in other axes

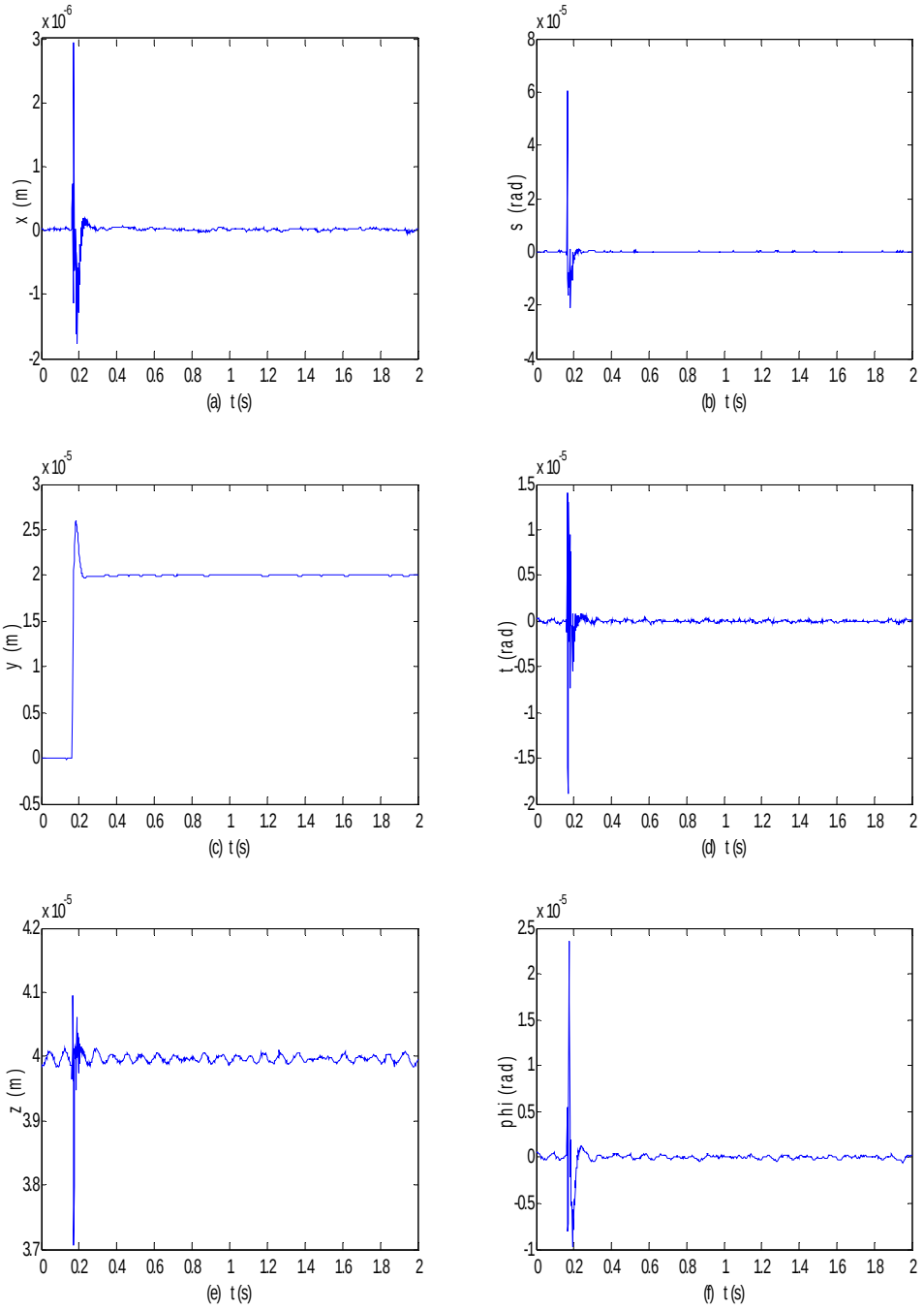

Figure 5-7 20-µm *y*-axis step response at a 40-µm levitation height with perturbations in other axes

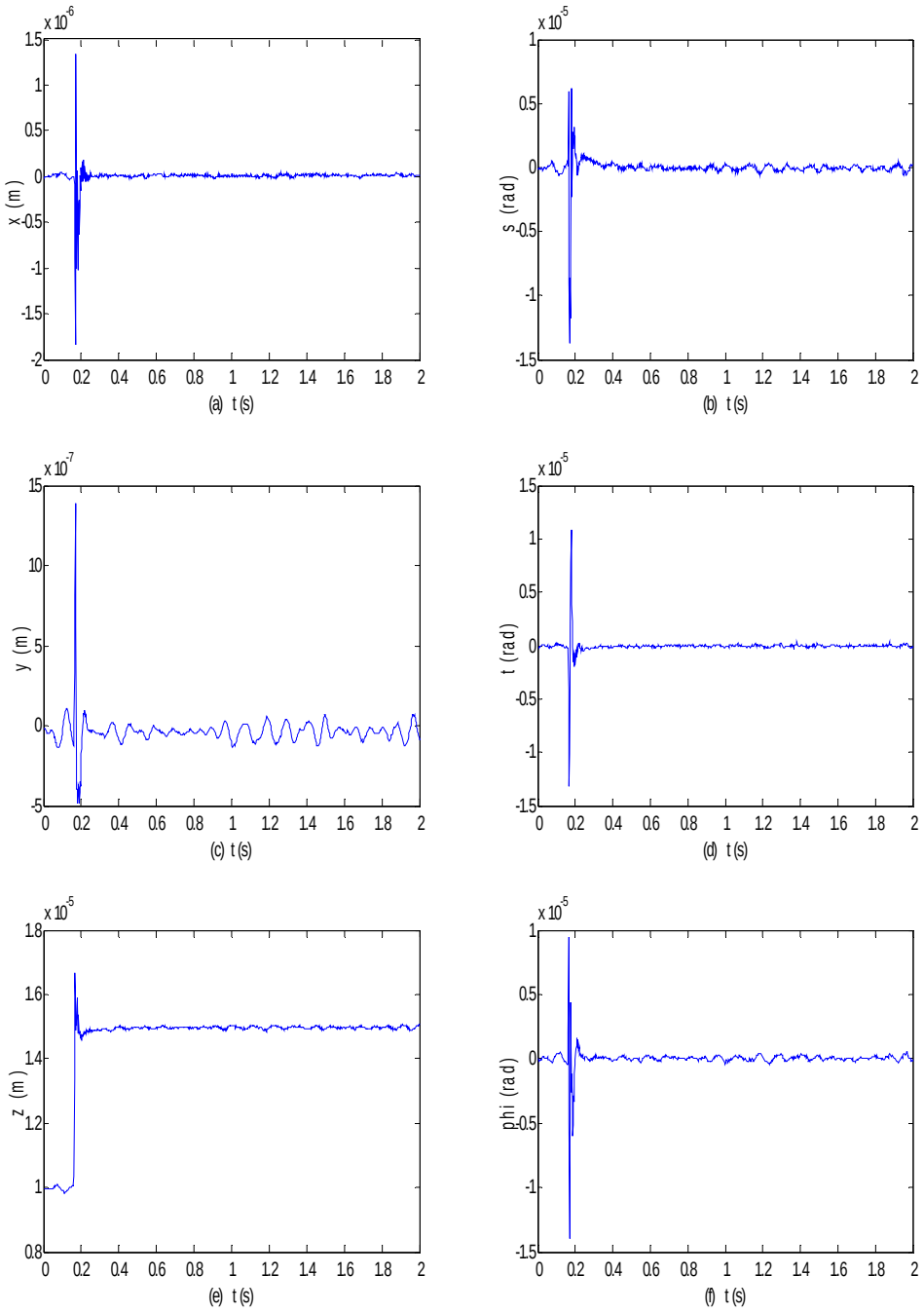

Figure 5-8 5-µm *z*-axis step response at a 10-µm levitation height with perturbations in other axes

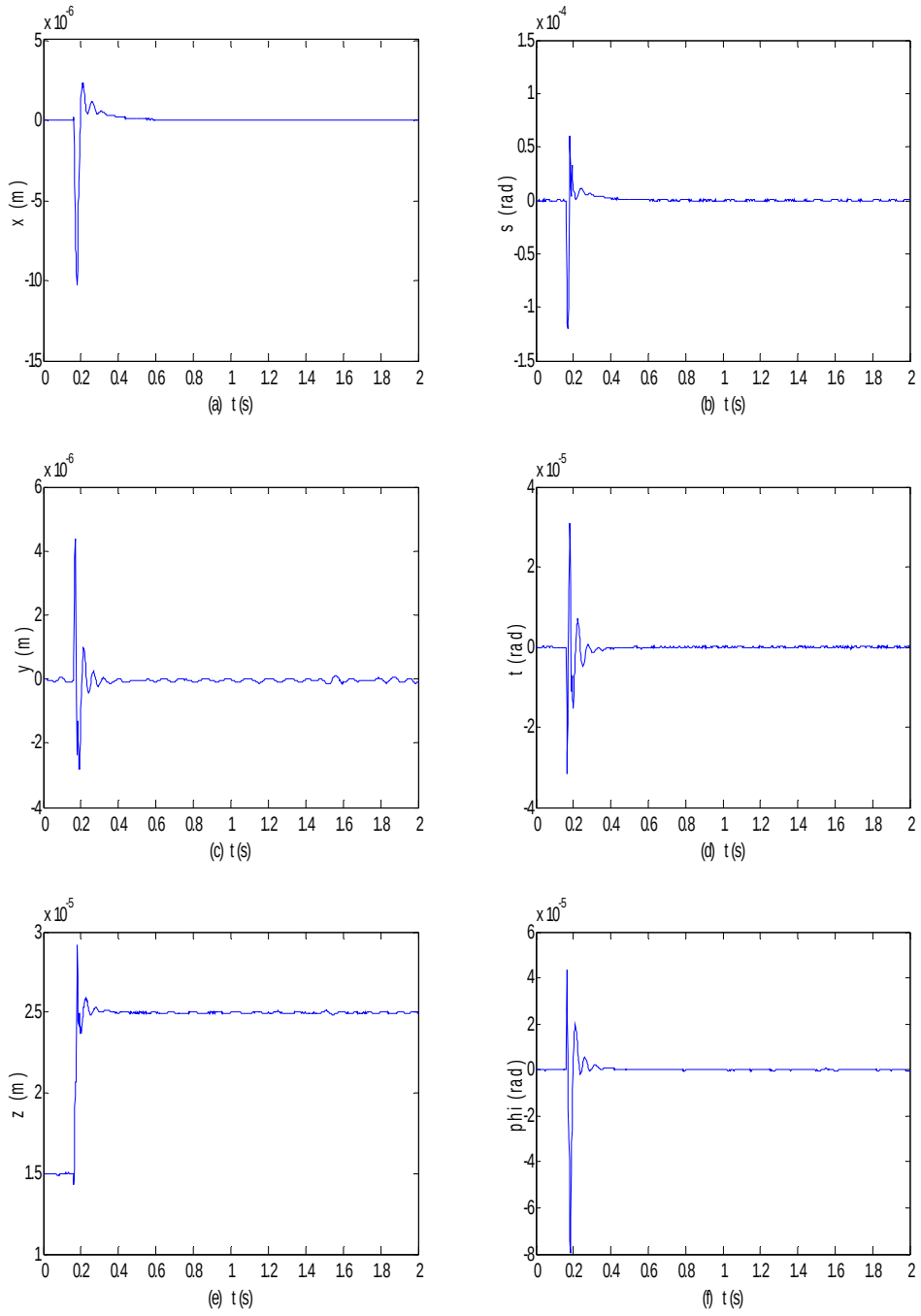

Figure 5-9 10-µm *z*-axis step response at a 15-µm levitation height with perturbation in other axes

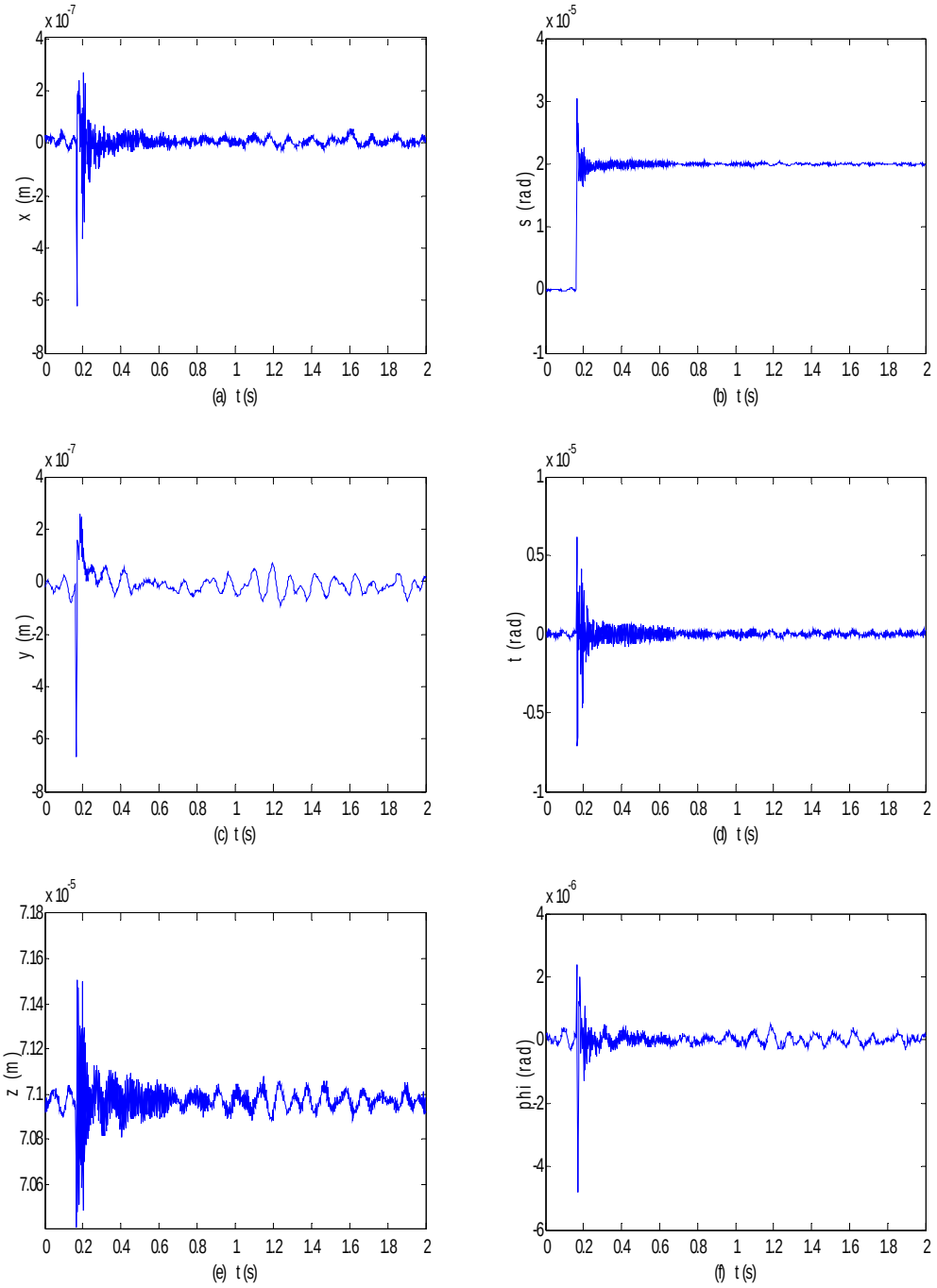

Figure 5-10 20-μrad θ-axis step response at a 71-μm levitation height with perturbation in other axes

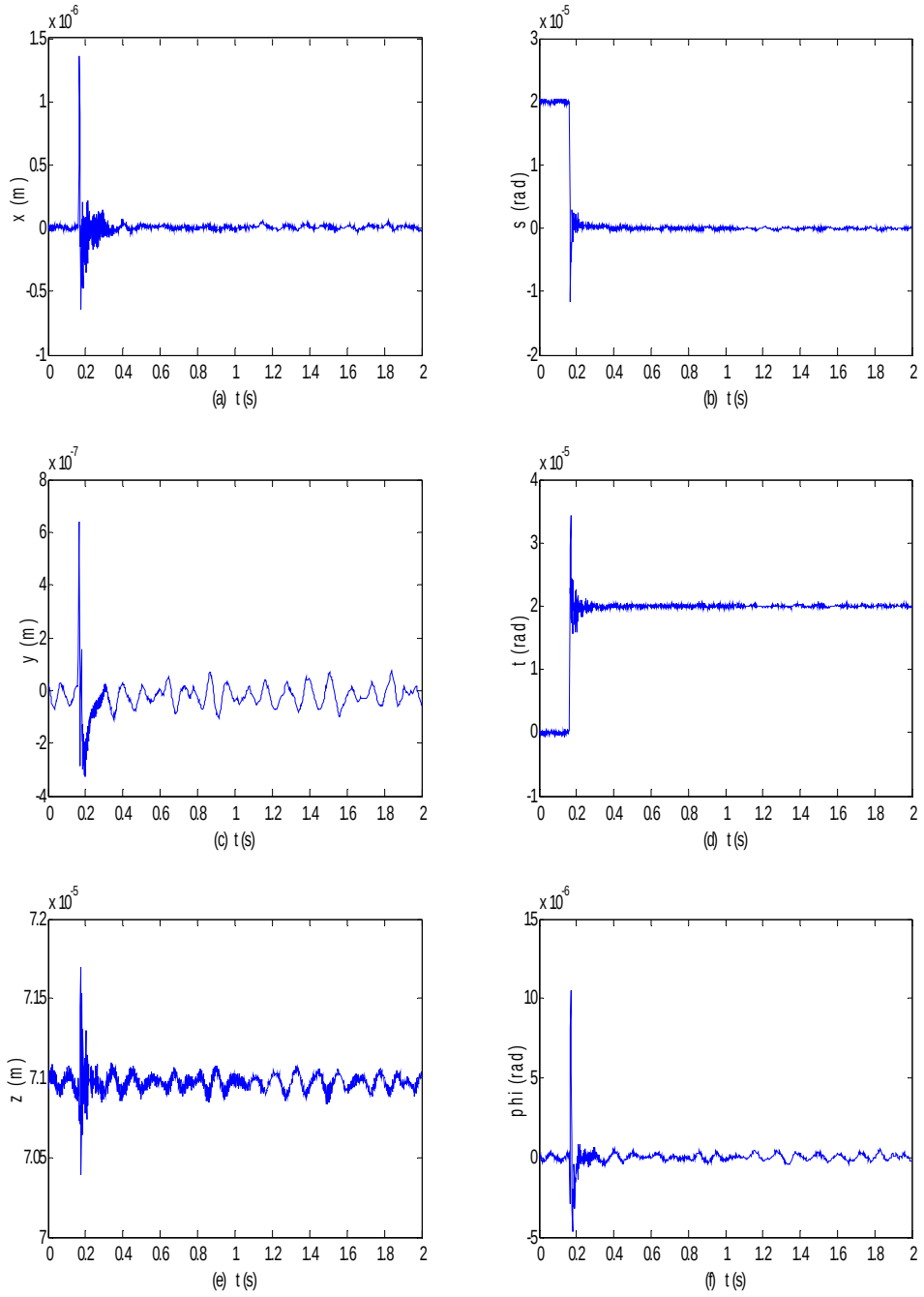

Figure 5-11 20-μrad φ -axis step response at a 71-μm levitation height with perturbation in other axes

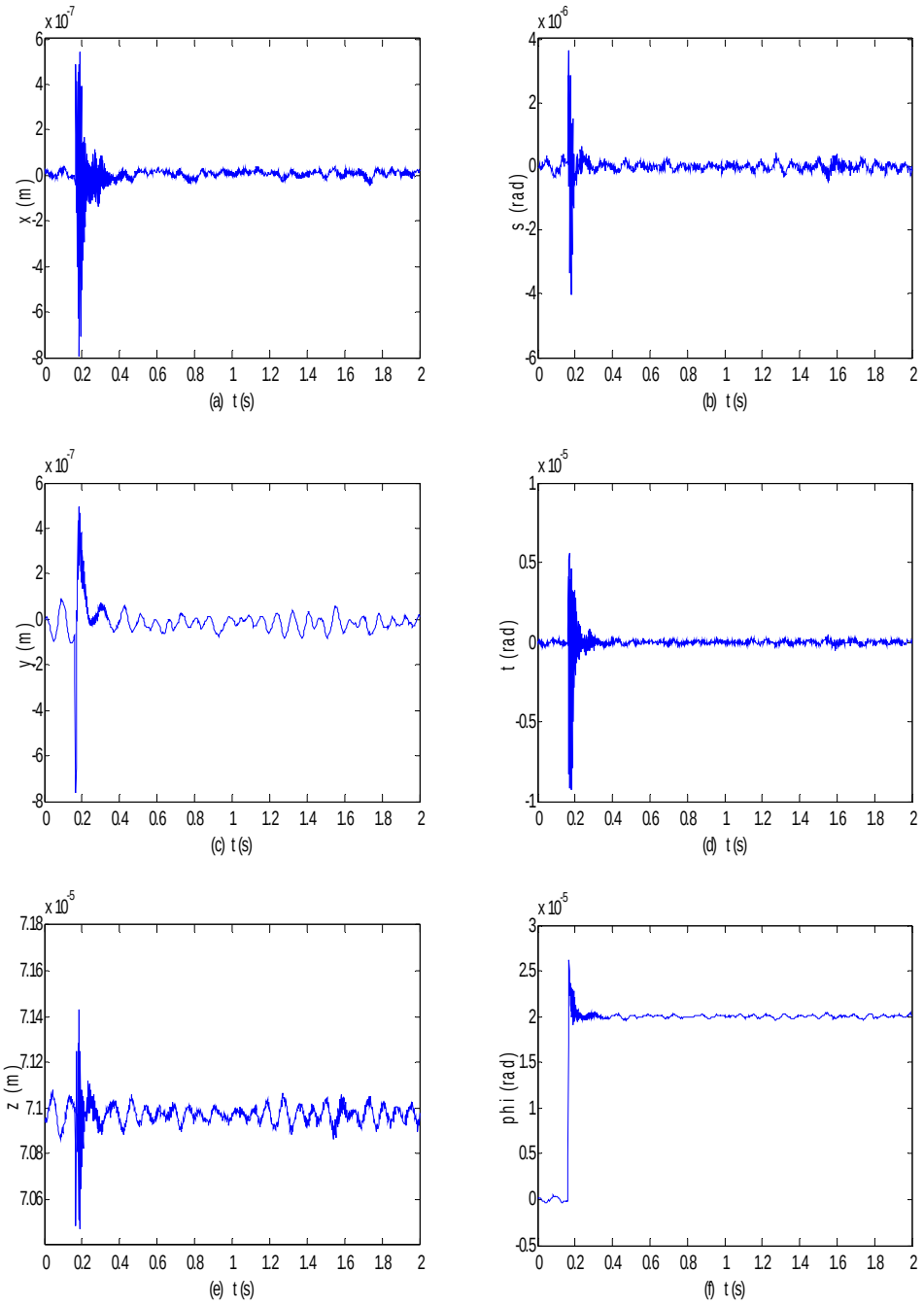

Figure 5-12 20-μrad ψ-axis step response at a 71-μm levitation height with perturbation in other axes

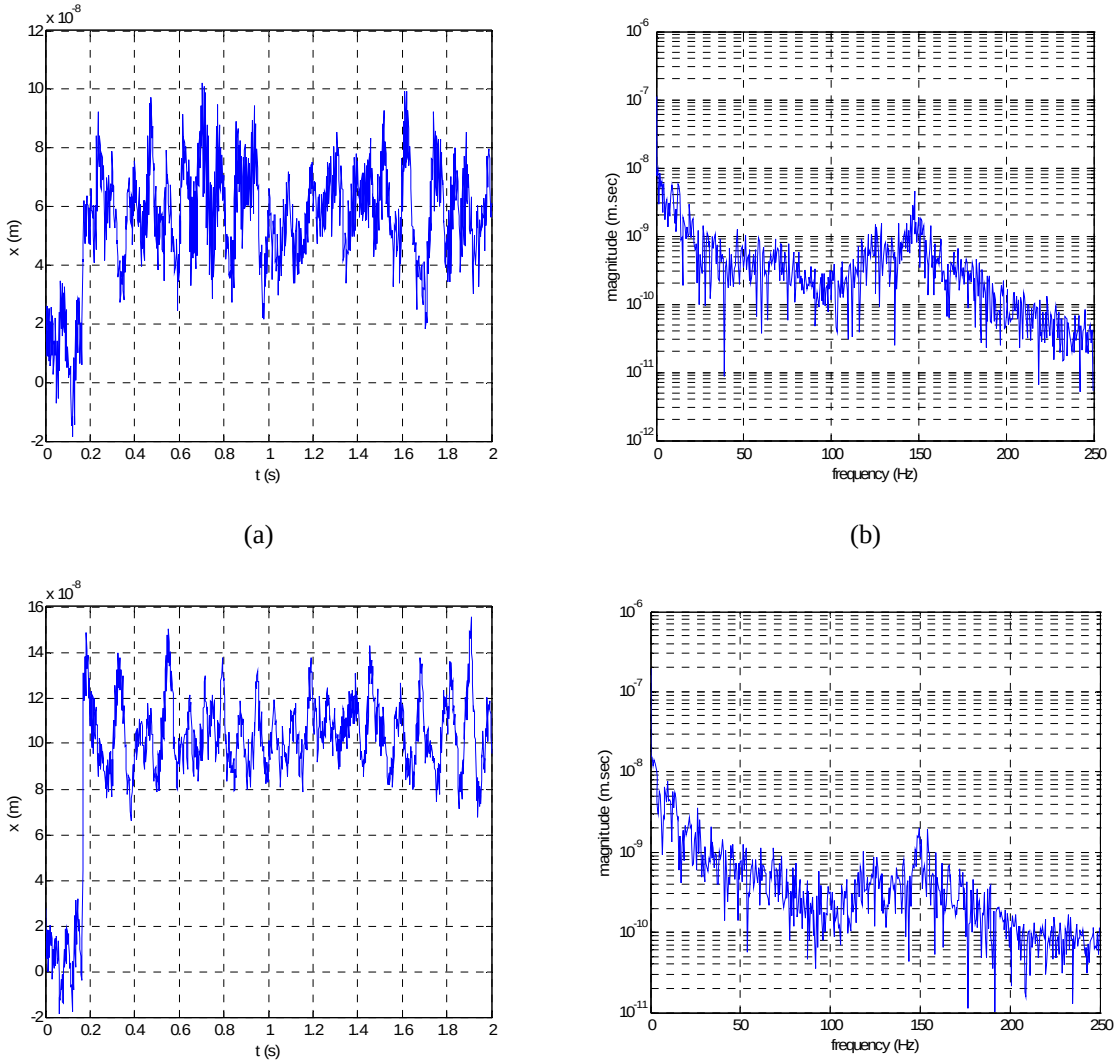

Figure 5-13 (a) 50-μm step response in *x* and (b) its FFT. (c) 100-μm step response in *x* and (d) its FFT.

5.3 Large-Range Trajectory Scanning Motions

Large-range trajectory scanning motion is common in precision applications such as microlithography. Several experimental results to demonstrate the 2-D and 3-D scanning capability of the positioner are presented in this section.

Figure 5-14 shows 5-mm planar circular and star-shape trajectories. The angular velocity was 0.5 rad/s in the circle and the linear velocity was 2.5 mm/s in the star-shape motion. Figure 5-

15 shows the 120 mm × 120 mm maximum range of the 6-DOF maglev positioner. The linear velocity is 2.5 mm/s in both *x*- and *y*-directions. The maximum travel range is supposed to be 160 mm × 160 mm, but the positioner would lose the laser beams and go unstable at the corners, outside of the range 120 mm × 120 mm. Figure 5-16 shows a 1-μm amplitude sinusoidal motion. This precision positioner can also move in the *z*-direction within the vertical distance sensor's range of 100 μm as well. Figure 5-17 shows the spring-shape of 3-dimension motion. It presents 7 circles of a 500-μm radius with a 2.3-rad/s angular velocity. The maximum velocity of 24.8 mm/s is presented in Figure 5-18. This is a part of back-and-forth motion with 10 mm steps in the *y*-direction. These experimental results prove that the 6-DOF positioner can be used multidimensional precision-positioning applications.

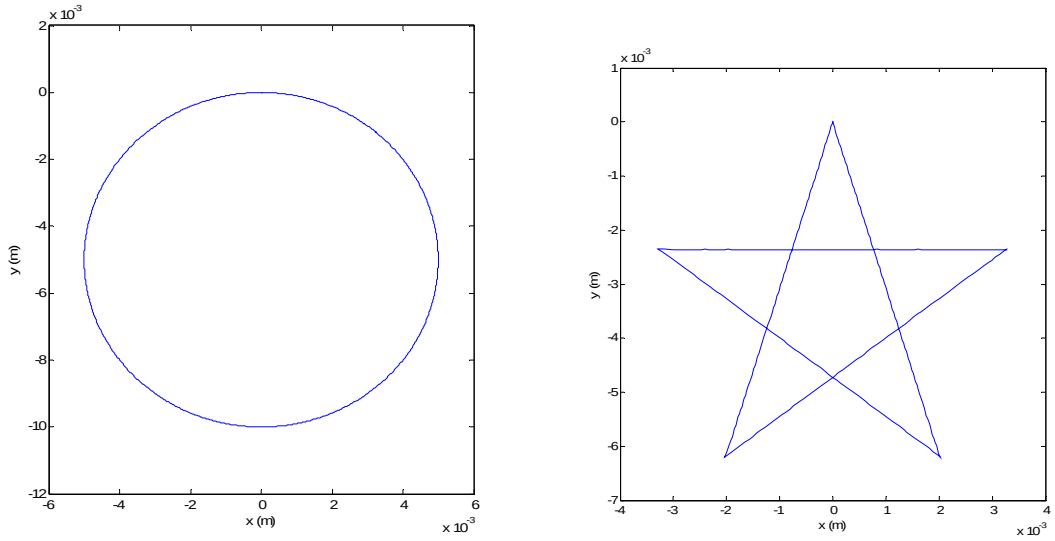

(a) (b)

Figure 5-14 Capability of following paths. (a) 5-mm radius circular motion (b) star-shape motion

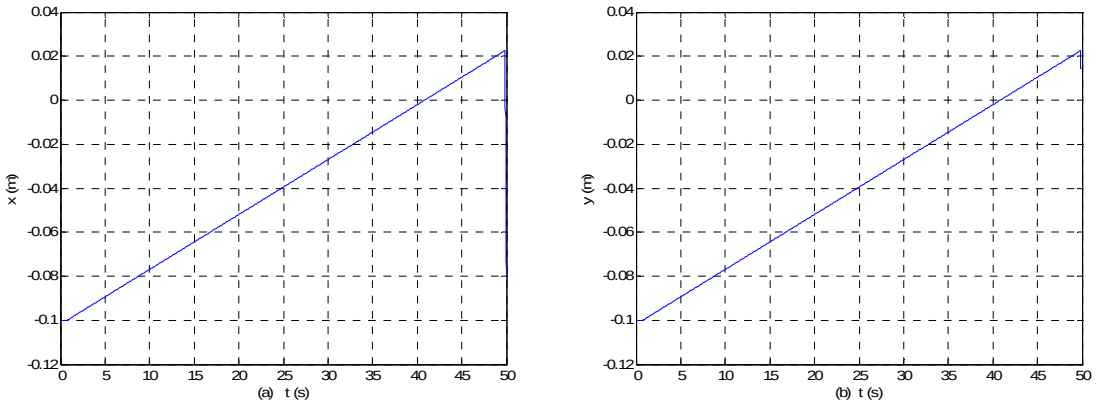

Figure 5-15 120-mm maximum travel range in (a) *x* and (b) *y*

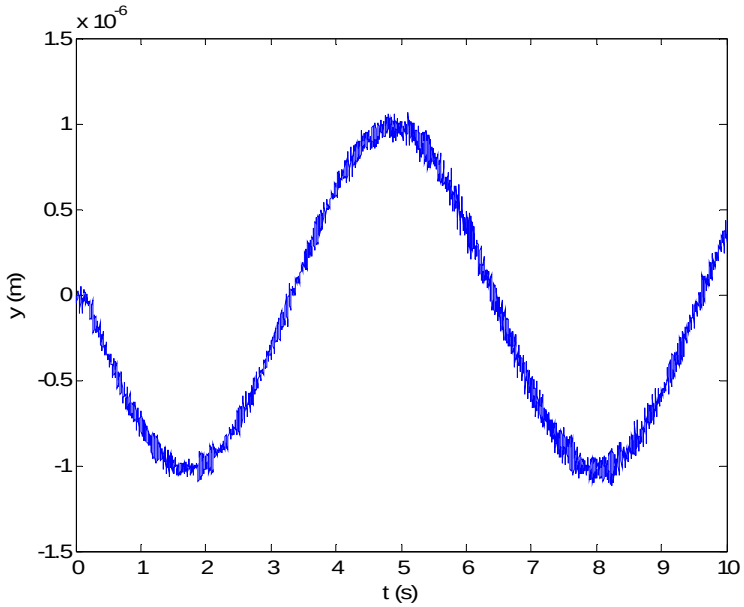

Figure 5-16 1-µm amplitude sinusoidal motion

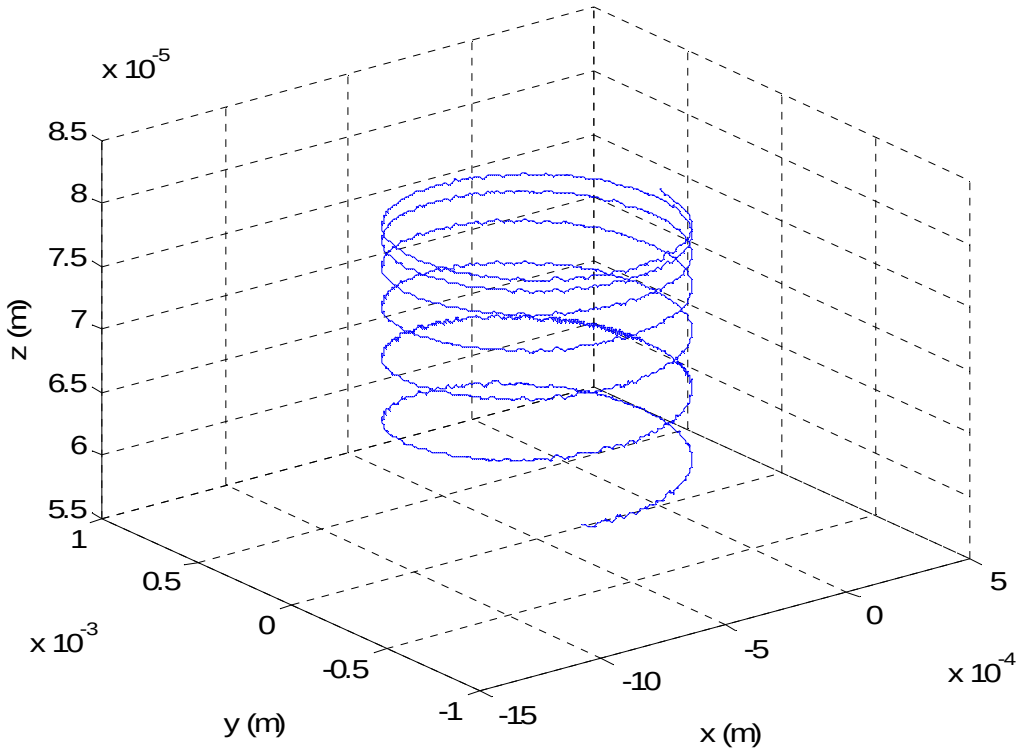

Figure 5-17 500-μm radius spring-shape trajectory in 3-D

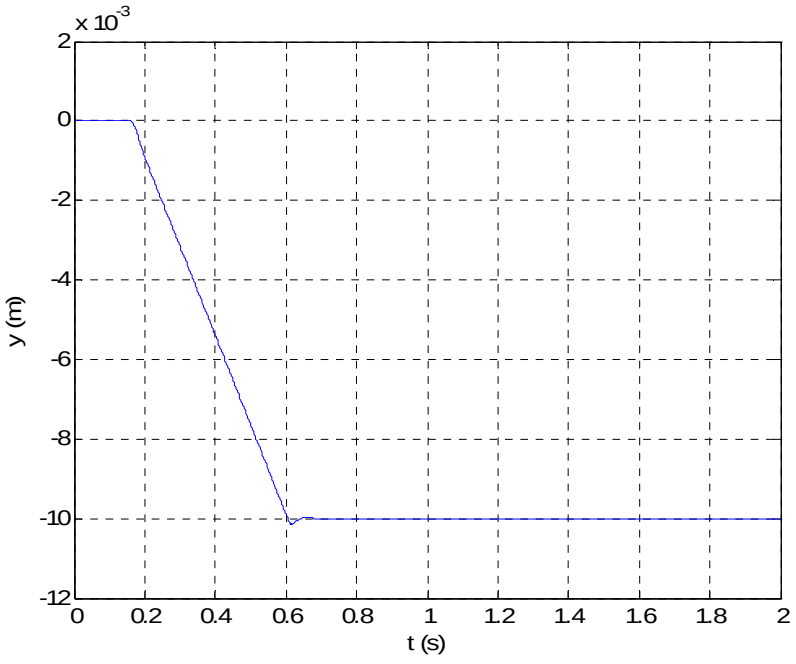

Figure 5-18 Velocity profiles in *y* with a 0.025-m/s maximum velocity

CHAPTER VI

CONCLUSIONS AND SUGGESTIONS FOR FUTURE WORK

In this chapter, the achievements in the controller design and implementation for the precision maglev positioner are discussed. Several suggestions for future work are also presented.

6.1 Conclusions

The 6-DOF high-precision maglev positioner consists of a single triangular moving platen with a 5.91 kg mass, a novel concentrated-field magnet matrix with the dimension of 304.8 mm × 304.8 mm × 12.7 mm, and three planar motors generating all 6-axis motions, three interferometers measuring 3-DOF horizontal platen motion with 0.6-nm resolution, three laser distance sensors measuring of 3-DOF vertical platen motion with 15-nm resolution, and a Pentek 4284 board with a TMS320C40 DSP performing real-time digital control. The only moving platen can generate all 6-axis fine and coarse motions including the stepping and large translational motions required in semiconductor manufacturing. In addition it can also generate 3-D motions. Furthermore, without mechanical contact the maglev stage requires no lubricant and produces no wear particles, so it is suited in clean-room environment. Because this precision positioner has a simple mechanical structure, its fabrication cost is not as high as that of other positioning systems.

The thesis presented digital controller design and implementation and several key experimental results with the 6-DOF high-precision maglev positioner. Dr. Won-jong Kim's former PhD student, Tiejun Hu, has obtained very good testing results with the integrated multidimensional positioner suspended with air-bearings. The purpose of this research was to

remove air-bearings, and levitate and control the platen with the magnetic forces only. The lateral motion controllers followed Hu's previous works, I designed and implemented the vertical motion controllers for *z*, *x*-rotation, and *y*-rotation in various experimental conditions. After each axis was stabilized, all of 6-axis motions were controlled in closed loop with magnetic forces. The sampling rate of the positioner was 5 kHz. The control bandwidth was 38 Hz in horizontal mode, 60 Hz in *z*, 40 Hz in θ, and 40 Hz in ψ by experiment. The maximum travel range is currently 120 mm × 120 mm. The positioner exhibits a 0.025-m/s maximum velocity. 5-μm, 10-μm, and 20-μm step responses in *x* and *y* were provided. A 5-mm radius circle, star-shape translation, micro-scale sinusoidal motion, and 500-μm radius sping-shape 3-D motions were also provided. This thesis demonstrated the utility of the high-precision maglev stage for nano- and micro-scale positioning applications.

6.2 Suggestions for Future Work

For an advanced high-precision positioner, several suggestions in mechanical and electrical aspects can be made. First, laser interferometery restricts the travel range of the positioner. Hall-effect sensors have no restriction to extend the travel range. They can also make the platen smaller replacing the bulky stick mirrors which reflect the laser beams. Second, the laser distance sensors for vertical position measurement have the measurement range of only 100 μm. If we use sensors that have a longer sensing range, the vertical motion range of the precision positioner may be extended. The current precision positioner sometimes exhibits instability because the dynamic coupling causes error motions out of the sensing range. Third, different shapes of the platen can be designed such as square as in [1]. A square platen with 4 planar motors may generate more stable motions with symmetry. Last, we can consider improvements in

materials and design. A lighter the platen will result in faster dynamics. Simplified power and sensor cables would also reduce immodeled.

REFERENCES

[1] T. Hu, “Design and control of a 6-degree-of-freedom levitated positioner with high precision,” PhD Dissertation, Texas A&M University, May 2005.

[2] G. Van Engelen and A. G. Bouwer, “Two-step positioning device using Lorentz forces and a static gas bearing,” U.S. Patent 5120034, June 1992.

[3] S. Sakino, E. Osanai, M. Negishi, M. Horikoshi, M. Inoue, and K. Ono, “Movement guiding mechanism,” U.S. Patent 5040431. August 1991.

[4] S. Wittekoek and A. G. Bouwer, “Displacement device, particularly for the photolithographic treament of a substrate,” U.S. Patent 4655594, April 1987.

[5] W.-J Kim, N. Bhat, and T. Hu, “Integrated multidimensional positioner for precision manufacturing,” *Journal of Engineering Manufacture*, vol. 218, no.4, pp.431–442, April 2004.

[6] W.-J. Kim, T. Hu, and N. Bhat, “Design and control of a 6-DOF positioner with high precision,” *Proceedings of 2003 ASME International Mechanical Engineering Conference and Exposition*, Paper No. 42780, November 2003.

[7] W.-J. Kim, “High-precision planar magnetic levitation,” PhD Dissertation, Massachusetts Institute of Technology, June 1997.

[8] D. L. Trumper, W.-J. Kim, and M. E. Williams, “Magnetic arrays,” U.S. Patent Office, Patent 5631618, May 1997.

[9] T. Asakawa, “Two dimensional positioning devices,” US Patent 4626749, December 1986.

[10] T. Asakawa, “Two dimensional precise positioning devices for use in a semiconductor apparatus,” U.S. Patent 4535278, August 1985.

[11] W. E. Hinds and B. Nocito, “The Sawyer linear motor,” *Proceedings of The Second Symposium on Incremental Motion Control Systems and Devices*, pp. W-1–W-10, 1973.

[12] E. R. Pelta, “Two axis sawyer motor for two-dimensional drive,” *IEEE Control Systems Magazine*, pp. 20–24, October 1987.

[13] N. Fujii and T. Kihara, “Surface induction motor for two-dimensional drive,” *J. Inst. Elect. Eng. Trans*., pp. 221–228, February 1998.

[14] A. Chitayat, “Two-axis motor with high density magnetic platen,” US Patent 5777402, July 1998.

[15] E. R. Pelta, “Two Axis Sawyer Motor,” *Proceedings of the 12th Annual IEEE Industrial Electronics Society Conference*, pp. 3–8, 1986.

[16] S. Verma, “Development of novel high-performance six-axis magnetically levitated instruments for nanoscale applications,” PhD Dissertation, Texas A&M University, August 2005.

[17] G. F. Franklin, J. D. Powell, and A. Emami-Naeini, *Feedback Control of Dynamic Systems*, 4th ed, Upper Saddle River, NJ: Prentice Hall, 2002.

[18] K. Ogata, *Modern Control Engineering*, 4th ed. Upper Saddle River, NJ: Prentice Hall 2002.

APPENDIX

REAL-TIME CONTROL C CODE

Lead-Lag Control Routine

```
#include "dsp.h"
#include "math.h"

void c_int01()
{
unsigned long D1reading;
long ADreading;
float z_mea;
int    i,j;

tr_low();
D1reading=*(unsigned long *)AD_FIFO_D1;
*(unsigned long int *)0xb0300003=0x0041;
    raw_x_pos=(*(long int *)0xb0300048 << 16) & 0xffff0000;
    raw_y1_pos=(*(long int *)0xb0310048 << 16) & 0xffff0000;
    raw_y2_pos=(*(long int *)0xb0320048 << 16) & 0xffff0000;

    raw_x_vel=(*(long int *)0xb030004e << 16) & 0xffff0000;
    raw_y1_vel=(*(long int *)0xb031004e << 16) & 0xffff0000;
    raw_y2_vel=(*(long int *)0xb032004e << 16) & 0xffff0000;

    tr_high();
    raw_x_pos|=((*(long int *)0xb0300048 >> 16) & 0x0000ffff);
    raw_y1_pos|=((*(long int *)0xb0310048 >> 16) & 0x0000ffff);
    raw_y2_pos|=((*(long int *)0xb0320048 >> 16) & 0x0000ffff);
    raw_x_vel|=((*(long int *)0xb030004e >> 16) & 0x0000ffff);
    raw_y1_vel|=((*(long int *)0xb031004e >> 16) & 0x0000ffff);
    raw_y2_vel|=((*(long int *)0xb032004e >> 16) & 0x0000ffff);
```

```
    x_pos=raw_x_pos*6.1815119987e-10;
    y1_pos=raw_y1_pos*6.1815119987e-10;
    y2_pos=raw_y2_pos*6.1815119987e-10;

    x_vel=raw_x_vel*3.77292037e-7;
        y1_vel=raw_y1_vel*3.77292037e-7;
    y2_vel=raw_y2_vel*3.77292037e-7;

tr_high();
ADreading=(*(unsigned long int *)AD_FIFO_A1>>16) & 0xffff;
if(ADreading & 0x8000)
ADreading = ADreading | 0xffff0000;
z_pos1=50e-6+ADreading*1.55389559450e-9;     /* 5/0x7fff*1.018e-
5=1.55389559450e-9 */

/*5/0x7fff=1.525925473799859614856410412915 4e-4*/
z_pos1 = z_pos1-z_pos10;
v1=ADreading*1.525925473799859614856410412915 4e-4;  /*voltage*/

ADreading=((*(unsigned long int *)AD_FIFO_B1>>16) & 0xffff);
if(ADreading & 0x8000)
ADreading = ADreading | 0xffff0000;
z_pos2=50e-6+ADreading*1.52898344068e-9;     /* 5/0x7fff*1.002e-
5=1.52898344068e-9*/
z_pos2 = z_pos2-z_pos20;
v2=ADreading*1.525925473799859614856410412915 4e-4; /*voltage*/

ADreading=((*(unsigned long int *)AD_FIFO_C1>>16) & 0xffff);
if(ADreading & 0x8000)
ADreading = ADreading | 0xffff0000;
z_pos3=50e-6+ADreading*1.53823132440e-9;     /* 5/0x7fff*5e-5=? */
z_pos3 = z_pos3-z_pos30;
v3=ADreading*1.525925473799859614856410412915 4e-4; /*voltage output--+-
3.8v out of range*/
tr_low();
```

```
yr=y1_pos;
xr=0.5773502692*y1_pos+1.1547005384*x_pos;
zr=0.3015*z_pos1+0.2889*z_pos2+0.4097*z_pos3;

rr=18.532*y2_pos;         /*17.8571 18.532*/
sr=z_pos1*-2.4097+z_pos2*4.6+z_pos3*-2.1903;
tr=z_pos1*-3.9455+z_pos2*0.1274+z_pos3*3.8182;

ur=y1_vel;                                  /*velocity*/
hr=0.5773502692*y1_vel+1.1547005384*x_vel;
vr=18.532*y2_vel;

cos_x=cos(123.25*xr);
cos_y=cos(123.25*yr);
sin_x=sin(123.25*xr);
sin_y=sin(123.25*yr);

if(demo_enable==1)
{
   t+=0.0002;
   switch(time_count)
   {
      case 1:
      {
       if(yr<=-1e-2)
        demo_enable=0;
       if(t>=0.0004)
        {
          t=0;
         yc-=10e-6;
         /*zc+=1e-7; */
         /* xc-=2e-6;  */
        }
        break;
      }
```

```
case -1:
{
 if(yr>=0)
  demo_enable=0;
 if(t>=0.0004)
  {
    t=0;
    yc+=1e-6;
    /*xc+=1e-6;*/ /*1.154700538e-6;*/
  }
  break;
}
case 2:
{
 if(xr<=-11e-2)      /*-11e*/
  demo_enable=0;
 if(t>=0.0004)
  {
    t=0;
  /*  yc-=1e-6;*/
    xc-=2e-6;
  }
  break;
}
case -2:
{
 if(xr>=3e-2)
  demo_enable=0;
 if(t>=0.0004)
  {
    t=0;
   /* yc=0;*/
    xc+=2e-6;
  }
  break;
}
```

```
case 3:  /* spiral circle */
{
if(step>5*6.28)
 demo_enable=0;
if(t>=0.0004)
 {
  t=0;
  step+=3e-4;
  if(step<5*6.28)
  {
   xc=-0.2e-2*(step/10)*(1-cos(step));
   yc=-0.2e-2*(step/10)*sin(step);
   /*zc-=1e-10*(step/10);  */
  }
 }
 break;
}
 case 12:
{
if(step>6.28)
 demo_enable=0;
if(t>=0.0004)
 {
  t=0;
  step+=2e-4;
  if(step<6.28)
  {
   xc=-0.5e-2*(1-cos(step));
   yc=-0.5e-2*sin(step);
  }
 }
 break;
}
case 4:   /* y- sinusoidal motion */
{
if(step>2*6.28)
```

```
      demo_enable=0;
      if(t>=0.004)
       {
        t=0;
        step+=2e-4;
        if(step<2*6.28)
        {
         xc=-1e-3*(1-cos(step));
         yc=-1e-3*sin(step);
        }
       }
        break;
      }
       case -5:
      {
       if(t>3)
        {
         demo_enable=0;
        }
       if(t<=0.1) yc=0.03-2.5*t*t;
       else if(t>0.1&&t<=0.28) yc=0.005-0.5*(t-0.1);
       else if(t>0.28&&t<=0.38) yc=-0.085-0.5*(t-0.28)+2.5*(t-0.28)*(t-
0.28);
/*       if(t<=0.1) yc=0.03-3*t*t;
       else if(t>0.1&&t<=0.22) yc=-0.6*(t-0.1);
       else if(t>0.22&&t<=0.32) yc=-0.072-0.6*(t-0.22)+3*(t-0.22)*(t-
0.22); */
 /*      if(t<=0.1) yc=0.03-3.5*t*t;
       else if(t>0.1&&t<=0.2) yc=-0.005-0.7*(t-0.1);
       else if(t>0.2&&t<=0.3) yc=-0.075-0.7*(t-0.2)+3.5*(t-0.2)*(t-0.2);
      if(t<=0.2) yc=0.03-1*t*t;
       else if(t>0.2&&t<=0.35) yc=-0.01-0.4*(t-0.2);
       else if(t>0.35&&t<=0.55) yc=-0.07-0.4*(t-0.35)+(t-0.35)*(t-
0.35);*/
       break;
      }
```

```
 case 5:
{
 if(t>0.02&&t<=1.256067977)
  {
    xc-=0.5*1e-6;
    yc+=0.5*0.324919696e-6;
  }
 if(t>1.27607977&&t<=2.327541994)
  {
   xc+=0.5*0.726542528e-6;
   yc-=0.5*1e-6;
  }
 if(t>2.347541994&&t<=3.647220778)
  {
   yc+=0.5*1e-6;
  }
 if(t>3.667220778&&t<=4.718683002)
  {
   xc-=0.5*0.726542528e-6;
   yc-=0.5*1e-6;
  }
 if(t>4.738683002&&t<=5.974750979)
  {
   xc+=0.5*1e-6;
   yc+=0.5*0.324919696e-6;
  }
 if(t>4.738683002&&t<=4.758683002)
  {
   zc+=0.5*1e-8;
  }
 if(t>4.778683002&&t<=6.014750979)
  {
    xc-=0.5*1e-6;
    yc+=0.5*0.324919696e-6;
  }
 if(t>6.034750979&&t<=7.086213203)
```

```
 {
  xc+=0.5*0.726542528e-6;
  yc-=0.5*1e-6;
 }
if(t>7.106213203&&t<=8.405891987)
 {
  yc+=0.5*1e-6;
 }
if(t>38.425891987&&t<=9.477354211)
 {
  xc-=0.5*0.726542528e-6;
  yc-=0.5*1e-6;
 }
if(t>9.497354211&&t<=10.73342219)
 {
  xc+=0.5*1e-6;
  yc+=0.5*0.324919696e-6;
 }
if(t>10.73342219)
 {
  demo_enable=0;
  t=0;
 }
 break;
}
 case 6:
{
if(step>20*6.28)
 demo_enable=0;
if(t>=0.0004)
 {
 t=0;
 step+=100e-4;
 if(step<20*6.28)
  {
   xc=-0.5e-3*(1-cos(step));
```

```
   yc=-0.5e-3*sin(step);
   zc-=2e-14;
  }
 }
 break;
}
case 7:
{
 if(t>0.02&&t<=15)
  {
    xc-=1e-6;
  }
 if(t>17.02&&t<=32)
  {
   xc+=1e-6;
   yc-=1e-6;
  }
 if(t>34.02&&t<=49)
  {
   xc-=1e-6;
  }
 if(t>51.02&&t<=66)
  {
   xc+=1e-6;
   yc+=1e-6;
  }
 if(t>66)
  {
   demo_enable=0;
   t=0;
  }
  break;
}

case 8:
{
```

```
 if(t>5)
 {
   demo_enable=0;
   t=0;
 }
 if(t<=0.1) yc=-0.5*t*t;
 else if(t>0.2&&t<=0.5) yc=-0.02-0.2*(t-0.2);

         break;
        }

case 9:    /*nano stair*/
{
 if(t>0.2&&t<=0.6)
  {
    yc=60e-9;
  }
 if(t>0.6&&t<=1.0)
  {
    yc=120e-9;
  }
 if(t>1.0&&t<=1.4)
  {
    yc=180e-9;
  }
 if(t>1.4&&t<=1.8)
  {
    yc=120e-9;
  }
 if(t>1.8&&t<=2.2)
  {
    yc=60e-9;
  }
 if(t>2.2&&t<2.6)
  {
    yc=0;
```

```
        }
       if(t>4)
        {
         demo_enable=0;
         t=0;
        }
        break;
      }
       case 10:    /*step and settle*/
      {
       if(t<=0.05) yc=-2*t*t;
       else if(t>0.05&&t<=0.1) yc=-0.005-0.2*(t-0.05);
       else if(t>0.1&&t<=0.15) yc=-0.015-0.2*(t-0.1)+2*(t-0.1)*(t-0.1);

       else if(t>1.15&&t<=1.2) yc=-0.02-2*(t-1.15)*(t-1.15);
       else if(t>1.2&&t<=1.25) yc=-0.025-0.2*(t-1.2);
       else if(t>1.25&&t<=1.3) yc=-0.035-0.2*(t-1.25)+2*(t-1.25)*(t-
1.25);

       else if(t>2.3&&t<=2.35) yc=-0.04-2*(t-2.3)*(t-2.3);
       else if(t>2.35&&t<=2.4) yc=-0.045-0.2*(t-2.35);
       else if(t>2.4&&t<=2.45) yc=-0.055-0.2*(t-2.4)+2*(t-2.4)*(t-2.4);
/*
       else if(t>3&&t<=4) xc=0;
       else if(t>5&&t<=5.05) xc=-(t-5)*(t-5);
       else if(t>5.05&&t<=5.1) xc=-0.0025-0.1*(t-5.05);
       else if(t>5.1&&t<=5.15) xc=-0.0075-0.1*(t-5.1)+(t-5.1)*(t-5.1);
*/
                else if(t>3&&t<=5) xc-=1e-6;

       else if(t>6&&t<=6.05) yc=-0.06+2*(t-6)*(t-6);
       else if(t>6.05&&t<=6.1) yc=-0.055+0.2*(t-6.05);
       else if(t>6.1&&t<=6.15) yc=-0.045+0.2*(t-6.1)-2*(t-6.1)*(t-6.1);

       else if(t>7&&t<=7.05) yc=-0.04+2*(t-7)*(t-7);
       else if(t>7.05&&t<=7.1) yc=-0.035+0.2*(t-7.05);
```

```
      else if(t>7.1&&t<=7.15) yc=-0.025+0.2*(t-7.1)-2*(t-7.1)*(t-7.1);

      else if(t>8&&t<=8.05) yc=-0.02+2*(t-8)*(t-8);
      else if(t>8.05&&t<=8.1) yc=-0.015+0.2*(t-8.05);
      else if(t>8.1&&t<=8.15) yc=-0.005+0.2*(t-8.1)-2*(t-8.1)*(t-8.1);

      else if(t>9&&t<=11) xc-=1e-6;

      if(t>12&&t<=12.05) yc=-2*(t-12)*(t-12);
      else if(t>12.05&&t<=12.1) yc=-0.005-0.2*(t-12.05);
      else if(t>12.1&&t<=12.15) yc=-0.015-0.2*(t-12.1)+2*(t-12.1)*(t-
12.1);

      else if(t>13&&t<=13.05) yc=-0.02-2*(t-13)*(t-13);
      else if(t>13.05&&t<=13.1) yc=-0.025-0.2*(t-13.05);
      else if(t>13.1&&t<=13.15) yc=-0.035-0.2*(t-13.1)+2*(t-13.1)*(t-
13.1);

      else if(t>14&&t<=14.05) yc=-0.04-2*(t-14)*(t-14);
      else if(t>14.05&&t<=14.1) yc=-0.045-0.2*(t-14.05);
      else if(t>14.1&&t<=14.15) yc=-0.055-0.2*(t-14.1)+2*(t-14.1)*(t-
14.1);

      else if(t>15&&t<=17) xc-=1e-6;

      else if(t>18&&t<=18.05) yc=-0.06+2*(t-18)*(t-18);
      else if(t>18.05&&t<=18.1) yc=-0.055+0.2*(t-18.05);
      else if(t>18.1&&t<=18.15) yc=-0.045+0.2*(t-18.1)-2*(t-18.1)*(t-
18.1);

      else if(t>19&&t<=19.05) yc=-0.04+2*(t-19)*(t-19);
      else if(t>19.05&&t<=19.1) yc=-0.035+0.2*(t-19.05);
      else if(t>19.1&&t<=19.15) yc=-0.025+0.2*(t-19.1)-2*(t-19.1)*(t-
19.1);

      else if(t>20&&t<=20.05) yc=-0.02+2*(t-20)*(t-20);
```

```
       else if(t>20.05&&t<=20.1) yc=-0.015+0.2*(t-20.05);
       else if(t>20.1&&t<=20.15) yc=-0.005+0.2*(t-20.1)-2*(t-20.1)*(t-
20.1);

       else if(t>21&&t<=27) xc+=1e-6;

       if(t>28)
        {
         demo_enable=0;
         t=0;
        }
        break;
      }
        }

}


/* controller */
if (controller_flag == 1)

{
er0x=xc-xr;
er0y=yc-yr;
er0r=rc-rr;

u0x=1.797*u1x-0.797*u2x+740000*(er0x-1.9882*er1x+0.98822*er2x);
/*21hz,pm=50*/
/*u0x=1.7854*u1x-0.7854*u2x+2871875*(er0x-1.9698*er1x+0.96986*er2x);  */
/*70 Hz */
/*u0x=1.7585*u1x-0.7585*u2x+3712816*(er0x-1.9663*er1x+0.96636*er2x);  */
/*80 Hz */
/*u0x=1.7332*u1x-0.7332*u2x+4609007*(er0x-1.9628*er1x+0.96287*er2x);
*/   /*90 Hz */
/*u0x=1.7082*u1x-0.7082*u2x+5620974*(er0x-1.9595*er1x+0.95958*er2x);  */
/*100 Hz */
```

```
/*u0x=0;   */
u0y=1.797*u1y-0.797*u2y+740000*(er0y-1.9882*er1y+0.98822*er2y);
/*21hz,pm=50*/
/*u0y=1.7854*u1y-0.7854*u2y+2871875*(er0y-1.9698*er1y+0.96986*er2y);  */
/*70 Hz */
/*u0y=1.7585*u1y-0.7585*u2y+3712816*(er0y-1.9663*er1y+0.96636*er2y);
*/  /*80 Hz */
/*u0y=1.7332*u1y-0.7332*u2y+1609007*(er0y-1.9628*er1y+0.96287*er2y);
*/   /*90 Hz */
/*u0y=1.7082*u1y-0.7082*u2y+5620974*(er0y-1.9595*er1y+0.95958*er2y);  */
/*100 Hz */

u0r=1.797*u1r-0.797*u2r+13062.95*(er0r-1.9882*er1r+0.98822*er2r);
/*38hz,pm=62 good!!*/

fA=0.477*u0x+0.5*u0y-10.01*u0r;           /*0.1 -0.8477*u0x 0.7477*/
fB=-0.477*u0x+0.5*u0y+10.01*u0r;            /*-0.1 0.8477*u0x -0.7477*/
fC=u0x;

/*
fA=-0.82273*u0x+0.51452*u0y-9.75956*u0r;         /*-0.82273*/
/*fB=0.82273*u0x+0.48548*u0y+9.75956*u0r;
fC=u0x;
*/

if(z_control==33)
{
er0z=zc-zr;
er0s=sc-sr;
er0t=tc-tr;

/*new z-controller */
/*12182004*/
/*u0z=1.8712*u1z-0.8712*u2z+963949*(er0z-1.9807*er1z+0.98073*er2z);   */
/*40 Hz pm50 */
```

```
u0z=1.7911*u1z-0.7911*u2z+1963864.7729*(er0z-
1.9832*er1z+0.9832296*er2z);     /*50 Hz pm60 */
u0z=1.8129*u1z-0.8129*u2z+2130434*(er0z-1.9734*er1z+0.973492*er2z);
/*60 Hz pm50 */
u0z=1.7549*u1z-0.7549*u2z+2774600*(er0z-1.9852*er1z+0.9852256*er2z);
/*60 Hz pm60 */
/*u0z=1.7854*u1z-0.7854*u2z+2858059.2417*(er0z-
1.9698*er1z+0.9698564*er2z);   */   /*70 Hz pm50 */
/*u0z=1.7587*u1z-0.7587*u2z+3684135.9789*(er0z-
1.9663*er1z+0.9663634*er2z);   */   /*80 Hz pm50 */

/*122604 consider various spring constant*/
/*u0z=1.8129*u1z-0.8129*u2z+2132636.155*(er0z-
1.9734*er1z+0.9734492*er2z);   */   /*1000*/
/*u0z=1.8129*u1z-0.8129*u2z+2133221.6432*(er0z-
1.9734*er1z+0.9734492*er2z);   */   /*1500*/
/*u0z=1.8129*u1z-0.8129*u2z+2132672.6441*(er0z-
1.9734*er1z+0.9734492*er2z);   */   /*2000*/
/*u0z=1.8129*u1z-0.8129*u2z+2129192.1692*(er0z-
1.9734*er1z+0.9734492*er2z);   */   /*2500*/
/*u0z=1.8129*u1z-0.8129*u2z+2130445.6474*(er0z-
1.9734*er1z+0.9734492*er2z);    */  /*3000*/
/*u0z=1.8129*u1z-0.8129*u2z+2127710.613*(er0z-
1.9734*er1z+0.9734492*er2z);   */   /*3500*/
/*u0z=1.8129*u1z-0.8129*u2z+2125260.6663*(er0z-
1.9734*er1z+0.9734492*er2z);  */    /*4000*/
/*u0z=1.8129*u1z-0.8129*u2z+2122860.0527*(er0z-
1.9734*er1z+0.9734492*er2z);   */   /*4500*/
/*u0z=1.8129*u1z-0.8129*u2z+2124272.7543*(er0z-
1.9734*er1z+0.9734492*er2z);   */  /*5000*/
/*u0z=1.8129*u1z-0.8129*u2z+2106834.8278*(er0z-
1.9734*er1z+0.9734492*er2z);  */   /*10000*/
/*u0z=1.8129*u1z-0.8129*u2z+1883398.32*(er0z-
1.9734*er1z+0.9734492*er2z);  */   /*100000*/
/*u0z=1.8129*u1z-0.8129*u2z+346645.137*(er0z-
1.9734*er1z+0.9734492*er2z);  */   /*1000000*/
```

```
/*011705 consider various phase margin*/
/*u0z=1.8776*u1z-0.8776*u2z+1406554.6264*(er0z-
1.9572*er1z+0.9572816*er2z);  */   /*30  unstable*/
/*u0z=1.8508*u1z-0.8508*u2z+1706508.8959*(er0z-
1.9656*er1z+0.9636688*er2z);  */   /*40 unstable*/
/*u0z=1.7547*u1z-0.7547*u2z+2775390.1268*(er0z-
1.9807*er1z+0.9807346*er2z);   */  /*60*/
/*u0z=1.6521*u1z-0.6521*u2z+3922719.198*(er0z-
1.9875*er1z+0.98752184*er2z);  */   /*70*/

/*y-rotation */
/*12182004*/
/*u0t=1.9331*u1t-0.9331*u2t+1058.2084*(er0t-
1.9892*er1t+0.9892176*er2t);  */    /*20 Hz new*/
/*u0t=1.9016*u1t-0.9016*u2t+2332.7136*(er0t-
1.9851*er1t+0.9851258*er2t);   */   /*30 Hz new*/
u0t=1.8712*u1t-0.8712*u2t+4101*(er0t-1.9811*er1t+0.9811338*er2t);
/*40 Hz new*/
/*u0t=1.8292*u1t-0.8292*u2t+7173.0327*(er0t-
1.9859*er1t+0.9859242*er2t);   */   /*40 Hz new pm60*/
/*u0t=1.8415*u1t-0.8415*u2t+6357*(er0t-1.9772*er1t+0.9772416*er2t);   */
/*50 Hz new*/
/*u0t=1.8292*u1t-0.8292*u2t+8319.6817*(er0t-
1.9859*er1t+0.9859242*er2t);  */    /*50 Hz new pm60*/
/*u0t=1.8129*u1t-0.8129*u2t+9032*(er0t-1.9734*er1t+0.9734492*er2t);  */
/*60 Hz new*/
/*010505 consider a spring constant*/
/*u0s=1.8710*u1s-0.8710*u2s+3597.1285*(er0s-1.9810*er1s+0.981034*er2s);
*/    /*40 new Hz*/

/*x-rotation */
/*12182004*/
/*u0s=1.9331*u1s-0.9331*u2s+1403.9079*(er0s-
1.9892*er1s+0.9892176*er2s);  */    /*20 new Hz*/
```

```
/*u0s=1.9016*u1s-0.9016*u2s+3083.5344*(er0s-
1.9851*er1s+0.9851258*er2s);   */   /*30 new Hz*/
u0s=1.8712*u1s-0.8712*u2s+5434*(er0s-1.9811*er1s+0.9811338*er2s);
/*40 new Hz*/
/*u0s=1.8292*u1s-0.8292*u2s+5436.2893*(er0s-
1.9859*er1s+0.9859242*er2s);  */    /*40 new Hz pm60/  */
/*u0s=1.8415*u1s-0.8415*u2s+8378*(er0s-1.9772*er1s+0.9772416*er2s);  */
/*50 new Hz*/
/*u0s=1.8292*u1s-0.8292*u2s+11004.7845*(er0s-
1.9859*er1s+0.9859242*er2s);  */   /*50 Hz pm60*/
/*u0s=1.8129*u1s-0.8129*u2s+11901*(er0s-1.9734*er1s+0.9734492*er2s);
*/   /*60 new Hz*/
/*010505 consider a spring constant*/
/*u0s=1.8710*u1s-0.8710*u2s+4912.1082*(er0s-1.9810*er1s+0.981034*er2s);
*/   /*40 new Hz*/

fZA=0.34024*u0z-3.88602*u0s+9.75956*u0t;
fZB=0.31251*u0z-3.85715*u0s-9.75956*u0t;
fZC=0.34725*u0z+7.74316*u0s;
/*fZA=15;
fZB=15;
fZC=15;*/
i_Ad=fZA*f2ih;      /*-2 0.079116*/
i_Bd=fZB*f2ih;
i_Cd=fZC*f2ih;
}
if(z_control==0)
{
i_Ad=0;      /*-2 0.079116*/
i_Bd=0;
i_Cd=0;
}

i_Aq=fA*f2ih;
i_Bq=fB*f2ih;
i_Cq=fC*f2ih;
```

```
i_Aa=cos_y*i_Aq-sin_y*i_Ad;
i_Ba=cos_y*i_Bq-sin_y*i_Bd;
i_Ca=cos_x*i_Cq-sin_x*i_Cd;
i_Ab=sin_y*i_Aq+cos_y*i_Ad;
i_Bb=sin_y*i_Bq+cos_y*i_Bd;
i_Cb=sin_x*i_Cq+cos_x*i_Cd;
current_A[0][0]=i_Aa;
current_A[1][0]=0.5*i_Aa+0.8660254037844*i_Ab;
current_A[2][0]=-0.5*i_Aa+0.8660254037844*i_Ab;
current_B[0][0]=i_Ba;
current_B[1][0]=0.5*i_Ba+0.8660254037844*i_Bb;
current_B[2][0]=-0.5*i_Ba+0.8660254037844*i_Bb;
current_C[0][0]=i_Ca;
current_C[1][0]=0.5*i_Ca+0.8660254037844*i_Cb;
current_C[2][0]=-0.5*i_Ca+0.8660254037844*i_Cb;

for(j=0;j<3;j++)
{
        v[0][j]=0x800+0xfff*current_A[j][0]/(-2.6); /*(20*0.13)*/
        v[1][j]=0x800+0xfff*current_B[j][0]/(-2.6);
        v[2][j]=0x800+0xfff*current_C[j][0]/(-2.6);
}
}

 tr_low();

if(flag_d2a==1)
{
for(i=2;i>=0;i--)       /*i=0;i<3;i++*/
        for(j=0;j<3;j++)
                *(unsigned int *) DAC_DATA_Reg=v[i][j];
for(i=0;i<7;i++)
        *(unsigned int *) DAC_DATA_Reg=0x800;
}
```

```
if ((snap_begin==1)&&(snap_enable=1))
{
int_count++;
}

z1cer=z0cer;
z1r=z0r;
z1cr=z0cr;

s1cer=s0cer;
s1r=s0r;
s1cr=s0cr;

t1cer=t0cer;
t1r=t0r;
t1cr=t0cr;

u2z=u1z;
u1z=u0z;
er2z=er1z;
er1z=er0z;
u2s=u1s;
u1s=u0s;
er2s=er1s;
er1s=er0s;
u2t=u1t;
u1t=u0t;
er2t=er1t;
er1t=er0t;

u2x=u1x;
u1x=u0x;
er2x=er1x;
er1x=er0x;

u2y=u1y;
```

```
u1y=u0y;
er2y=er1y;
er1y=er0y;

u2r=u1r;
u1r=u0r;
er2r=er1r;
er1r=er0r;

display=1;
MX_Int_Clr= 0x20000029;
*(unsigned int *)MX_Int_Clr=0x0;

}
```

VITA

HO HU

Education

Texas A&M University, College Station, Texas. 2003-2005, Master of Science in Mechanical Engineering.

Hanyang University, Seoul, Korea. 1999-2003, Bachelor of Science in Mechanical Engineering. Thesis advisor: Jin-soo Cho

Address

Dongan-gu Pyongchon Life Apartment 108-602, Anyang Kyonggi, 431-070, Korea.